ISSN 1580-2949
UDK 669+666+678+53 MTAEC9, 42(3)97–139(2008)

MATER. TEHNOL.	LETNIK VOLUME 42	ŠTEV. NO. 3	STR. P. 97–139	LJUBLJANA SLOVENIJA	MAY-JUN. 2008

VSEBINA – CONTENTS

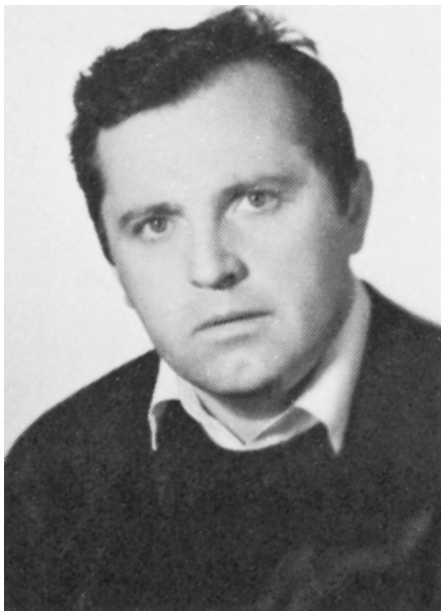

DR. BORISU ULETU V SPOMIN

Dr. Boris Ule je bil rojen v Ljubljani, kjer je obiskoval tehniško srednjo šolo metalurške stroke, se nato vpisal na študij metalurgije na Univerzi v Ljubljani, kjer je tudi magistriral in si pridobil najvišji akademski naslov doktor metalurških znanosti. Po končanem študiju se je zaposlil v industriji in si pridobil veliko izkušenj, ki so mu bile odlična osnova za kasnejše raziskovalno delo na Inštitutu za kovinske materiale in tehnologije.

Borisa sem spoznal pred 40 leti, ko smo se začeli kot bruci na metalurgiji seznanjati s kovinskimi materiali, tehnologijami in prvimi koraki pri raziskovalnem delu. Že v tistem času so ga zanimala nova spoznanja iz fizike in matematike, še posebej pa nova odkritja v vesolju, ki mu je posvetil veliko svojega prostega časa. V knjižnici, kjer smo skupaj preživeli veliko časa ob študiju, nas je s svojim duhovitim načinom, razgledanostjo in briljantnimi domislicami motiviral in spodbujal, da smo ob rednem študiju tudi sami začeli odkrivati različna interesna področja, ki smo jih kasneje v industriji oziroma v raziskovalnih organizacijah tudi razvili. Izjemni so bili večeri, ki smo jih po opravljenih izpitih preživeli pri Mraku, še posebej, ker smo tam redno srečevali tudi dramatika Ivana Mraka, ki ga je znal Boris, z vsem spoštovanjem do njega, neverjetno dobro posnemati. Iz študentskih dni mi je ostal v spominu "Skok čez kožo", ki smo ga v letu 1973 organizirali v hotelu Union in katerega duša je bil Boris. Takrat se še ni zavedal, da je storil prvi korak, ki mu je zaznamoval celotno njegovo življenje. V Belgiji - v Monsu, kamor so ga na "Skok čez kožo" povabili naši belgijski kolegi, je namreč dve leti pozneje spoznal ženo Lauro, ki mu je vse življenje dajala

DR. BORIS ULE: IN MEMORIAM

Boris ule was born in Ljubljana and graduated in metallurgy at the University of Ljubljana, where he received also the doctor degree in metallurgical science. He started the professional career in industry, where he acquired knowledge and experience that were later an excellent base for work in research and development in the Institute of Metals and Technology, Ljubljana.

I have known Boris for a number of years, since, we started to study metallurgy and metallic materials in the same class. He was a very good student and found great interest in the physics of metals and the mathematical description of processes and spent, also, plenty of free time to held himself acquainted with the newest findings related to Space. In the library, where we used to study before tests and examinations, he cheared frequently the atmosphere with witty remarks and jokes and helped to motivate the collegues for better comprehension of the studied matter. Not to be forgotten, after having passed with success different examinations, will remain the evenings in the tavern Pri Mraku, where we met sometimes the playwriter Ivan Mrak and Boris entertained the companionships with talented imitation of the writer's very typical poise and speaking.

From student years, I remember well the event "Skok čez kožo" we helped to organise in the hotel Union with Boris as motivating spirit. At a similar event in Mons in Belgium, where he was representing the associations of students of mining and metallurgy in Ljubljana, he met later the future spouse Laura, Together they upbrought two children and for Boris, the family and particularly the spouse, was a strong support in the decision of

trdno oporo, da je lahko po končani uspešni karieri v industriji veliko svoje energije usmeril v raziskovalno delo s področja fizikalne metalurgije na IMT.

Dve desetletji je bil vrhunski raziskovalec z občutkom za inženirsko delo in željo po novih spoznanjih, ki jih je dopolnjeval z odličnim znanjem fizike in matematike. Njegovo pionirsko delo na področju lomne mehanike je omogočilo kasnejši razvoj nestandardnih metod merjenja lomne žilavosti orodnih jekel. Ustanovil je Laboratorij za raziskave lezenja in razvijal metodike merjenja v mehaniki loma in pri lezenju, še zlasti z razvojem nestandardnih metod merjenja, povezanih z miniaturizacijo preizkušancev. V tem obdobju je eno študijsko leto predaval predmet Fizikalna metalurgija II na smeri Metalurgija in materiali na Naravoslovno-tehniški fakulteti Univerze v Ljubljani.

Po diagnosticirani bolezni se je z njemu lastno radovednostjo z njo v celoti seznanil in vse svoje sile usmeril v premagovanje le-te. Vsi, ki smo v zadnjem desetletju sodelovali in prijateljevali z njim, smo lahko občudovali njegov optimizem, vitalnost in delavnost, ki jo je usmeril v pisanje knjige z rešenimi nalogami iz Fizikalne metalurgije, ki je izšla v založbi IMT leta 2004. To kompleksno delo bo služilo še mnogim generacijam študentov, inženirjev in raziskovalcev za boljše razumevanje lastnosti kovinskih materialov in procesov, s katerimi lahko še oplemenitimo in izboljšamo njihove lastnosti. Velik pomen te knjige je tudi v izpiljeni slovenski strokovni terminologiji, ki bogati slovenski jezik in omogoča nedvoumno razumevanje strokovnih pojmov. V tem času je vedno našel dovolj energije in entuziazma, da je spodbujal in usmerjal mlade raziskovalce pri izdelavi njihovega doktorskega dela. Svoje raziskovalno delo je na strokovnih konferencah in v strokovnih revijah znal predstaviti širši domači in tuji strokovni javnosti in bil pogosto citiran. Njegova bibliografija obsega več kot 125 bibliografskih enot. Objavil je več deset znanstvenih člankov v priznani domači in tuji znanstveni periodiki. Vse to pa ne bi nikoli nastalo, če ga ne bi spodbujali in mu po svojih močeh pomagali njegovi najbližji.

O Borisu lahko rečem, da je bil dober kolega, nesebičen raziskovalec, predvsem pa velik prijatelj.

Zato, Boris, bom uporabil besede Abrahama Lincolna:

"And in the end, it's not the years in your life that count. It's the life in your years."

Vojteh Leskovšek

continuing his professional career in research in the Institute of Metals and Technology.

For two decades, Boris remained a central figure as researcher in the field of physical metallurgy he has developed and a strong support for collegues, especially for topics of research where a deeper knowledge in physics of metals and mathematics was necessary. His pioneer work in fracture mechanics was at the base for the later development of non standard methods of particular importance for tool and brittle steels. He helped in the establishnent of the laboratories for testing of creep and fracture mechanics and particularly in the use of small, non standard test specimens. In those years Boris teached for one year the course Physical metallurgy in his mother school, the Faculty of Natural Science and Technology of the University of Ljubljana.

With a characteristic candour and directness he studied first and than started to fight the malignant disease maintaining all the time a very high level od research activity. Friends and collegues, we admired his vitality, dynamism and optimism and the endeavour by writing the book on Solved Tasks in Physical Metallurgy that was printed in 2004 with IMT as editor. It is a valued book not only for students of metallic materials but also for teachers, particularly those working in physical metallurgy and chemistry of solids. The book will remain of ground importance for many generations of students, engineers and teachers, since, it helps not ony to understand better what metallic materials are, but also how to find quantitative answers with mathematical tools. The book is of great importance also as reference for Slovenian terminology for the field of metals and alloys and related topics.

Inspite of the progressing disease, Boris found always time and energy for writing and editing articles on original research findings that were printed in national and international scientific journals or presented at scientific conferences. His bibliography numbers 125 original articles representing a volume of excellent research work that would not be achieved without the maximal understanding and support from the family.

Boris will be remembered as good collegue, very good scientist and particularly as generous friend.

For You, Boris, I will quote the words of Abraham Lincoln:

"And in the end, it’s not the years in your life that count. It’s the life in your years."

Vojteh Leskovšek

UDK 539.42:669.14.018
Reviewed scientific article/Pregledni znanstveni članek

ISSN 1580-2949
MTAEC9, 42(3)99(2008)

ON THE DIFFERENT NATURE OF TIME-DEPENDENT AND TIME-INDEPENDENT IRREVERSIBLE DEFORMATION

O RAZLIČNI NARAVI ČASOVNO ODVISNE IN ČASOVNO NEODVISNE IREVERZIBILNE DEFORMACIJE

Leonid B. Getsov

Saint-Petersburg State Polytechnic University
guetsov@online.ru

Prejem rokopisa – received: 2007-04-06; sprejem za objavo – accepted for publication: 2008-02-15

Several current models for elastoviscoplasticity use irreversible deformations without dividing them into time-dependent and time-independent components. This article presents experimental data on the difference in the mode of deformation and in the fracture conditions compared to the actual values. General functional dependences are proposed for the description of the dependence of the material characteristics from the conditions of exposure to high temperature. The interference of creep deformation and momentary deformation in conditions of static and cyclic deformations is investigated. A method is proposed for summing the irreversible deformations, taking into account their difference in nature.

Key words: elastoviscoplasticity, ireversible deformation, time dependence, separation

Več sedanjih modelov elastoviskoplastičnosti uporablja irevezibilno deformacijo brez ločitve v časovno odvisno in v časovno neodvisno komponento. V tem članku so predstavljeni eksperimentalni podatki o tem, da lahko to povzroči pomembno razliko v načinu deformacije in v pogojih preloma. Predlagana je splošna funkcijska odvisnost za opis karakteristik materiala v odvinosti od pogojev obremenitve pri visoki temperaturi. Raziskavna je interferenca deformacije z lezenjem in trenutne deformacije v pogojih statične in ciklične deformacije. Predlagana je metoda za seštetje ireverzibilnih deformacij, ki upošteva razliko v njihovi naravi.

Ključne besede: elastoviskoplastičnost, ireverzibilna deformacija, časovna odvisnost, metoda ločitve obeh

1 INTRODUCTION

Some of the current models of plasticity consider time-dependent irreversible deformations separately from time-independent deformations[1]. At the same time, the parameters of a number of other models for plasticity are time-dependent components of the tensor of plastic deformation. This paper presents experimental data confirming that in a number of cases it is not correct to use the second approach and it is more appropriate to use the models of thermoelastoviscoplasticity (and thermo-viscoelastoplasticity, according to the classification of Perzyna[2]) and the division of irreversible deformations into time-dependent and time-independent components. It should be noted that the question about such divisibility (on the basis of the notion of momentary deformation curves introduced by Yu. N. Rabotnov) was resolved positively in experimental studies of different alloys based on iron and nickel. The results of an experimental study pertaining the conditions of a uniaxial stress state were observed mainly for heat-resistant steels and alloys.

2 MICROSTRUCTURAL PECULIARITIES OF DEFORMATION PROCESSES

It is known that because of the different crystallographic orientation of the grains in polycrystalline metal materials, microstresses in such materials differ considerably (also because of the anisotropy of the coefficient of elasticity) from the average stresses both by the value and by the direction of the deviator vector. For this reason, the microplastic deformations differ considerably in terms of value from the average deformation and this induces residual stresses usually referred to as residual stresses of type II, which cause the Bauschinger effect and plastic hysteresis. It is evident that the time-independent microplastic deformations and microcreep deformations may take place both when deforming with stresses higher and lower than the elastic limit and may produce the relaxation of internal stresses of type II. B. I. Rovinsky and V. G. Liuttsau[4] have linked the processes of micro- and macrocreep and have shown that the character of the process of microstress relaxation was similar to that of macrostress relaxation.

Which deformations, microplastic or microcreep, are larger in magnitude in conditions of stresses under the elastic limit (σ_y), including cyclic stresses, is the question that can only be answered on the basis of experimental results. It is known, as proved by the analysis of data on the microdeformations of different materials under single loading[5], that at low temperatures the microplastic deformations are considerably larger. However, in the case of cyclic deformation the process of development of microplastic deformations in many materials is slowed as the number of cycles increases, whereas the rate of accumulation of microcreep deformations under cyclic

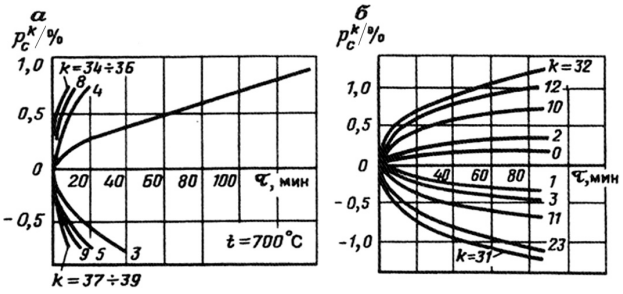

Figure 1: Cyclic creep curves for the alloy EI765 at 700 °C. (a) hard loading cycle, (b) soft loading cycle,
a) τ_c = 290 MPa, $\Delta\varepsilon$ = 1,2 %; b) τ_c = 272 MPa (τ_c – elastic limit)
Slika 1: Krivulje cikličnega lezenja za zlitino EI 765 pri 700 °C. (a) cikel trde obremenitve, (b) cikel mehke obremenitve

alternating loading increases with the number of cycles (**Figure 1**). At high temperatures the microcreep deformations are considerably larger than the microplastic deformations.

These conclusions were confirmed by the author's electron microscope observations of the deformation relief on heat-resistant alloy samples with precipitation strengthening after momentary tension in vacuum under high temperature up to stresses that were considerably lower than the elastic limit (a), after keeping it in such conditions for a short period of time (b) and after a creep test (c). After unloading, the deformation relief of the alloy EI826 (ChN70WMTAlV) formed at 850 °C was investigated after momentary and prolonged loading up to σ = 220 MPa – 0.6 σ_c (**Figure 2**). After a longer loading time (1–4 h) and a creep test, the accumulation of a microcreep deformation of 0.1 % and the intense development of fine slip lines were discovered in the overwhelming majority of grains. (**Figure 2b**). By difference, in conditions of momentary loading (with a rate of 180–2400 %/h) after loading-unloading the packets of slip lines were found in only 30 % of grains (**Figure 2a**).

Particles of the second phase in heat-resistant alloys are efficient barriers for the development of conservative sliding and can be overcome with microplastic deformation only at high stress with the mechanisms of lateral sliding and cutting. At the same time, during prolonged loading at the stress $\sigma < \sigma_e$, the accumulation of creep deformation is controlled by dislocation creep over barriers. Besides, unlike the case of momentary loading, where shearing of grain boundaries (because of the strong off-orientation of the lattice) is not possible, by creep deformation inter-grain sliding may also occur and cause the accumulation of creep damage.

Thus, the analysis of the microstructural behavior of materials during deformation shows that it is useful to divide irreversible deformation into creep deformation and time-independent plastic deformation.

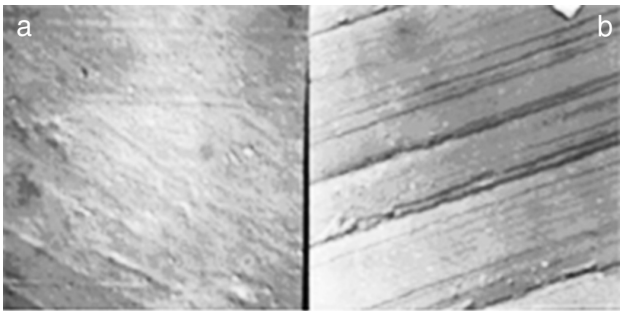

Figure 2: Microstructure of the alloy EI826 after momentary loading (a) and after prolonged loading (b) σ = 220 MPa at 850 °C
Slika 2: Mikrostruktura zlitine EI 826 po trenutni (a) in po podaljšani (b) obremenitvi

3 CREEP DEFORMATION CAPACITY OF MATERIALS

The deformation accumulated in a material at the moment of rupture, is, as a rule, considerably different in the cases for momentary loading and after a creep test. As an example, in **Table 1** the values of the residual elongation for two groups of steels and alloys after a short time deformation up to rupture and after long-term strength tests (in creep conditions) are shown. The alloys of group A have values close to the residual elongation after short-term tension and after a long-term strength test. This confirms the conclusion, considering the deformation at rupture, that for the materials of group B the equal residual deformation accumulated by momentary loading (ε) and in creep (p), may lead to considerably different values of damage ($\varepsilon/\varepsilon_f$ and p/ε_c). Thus, for such materials, the use of irreversible deformations without the separation into time-dependent and time-independent deformations may produce considerable errors in the determination of the margins of safety.

Table 1: Residual elongation after creep and after momentary loading
Tabela 1: Sposobnost za deformacijo v primeru lezenja in trenutne obremenitve

Material	Group	Temperature, °C	Residual elongation (%) under	
			Long-time rupture (100–1000 h)	Momentary tension
22*K*	A	500	21–23	24
15ChM		520	15–31	21
12Ch1MV		500	34–41	21–22
10Ch18N10T		650	9–45	27–37
25Ch2M1V	B	550	1,0	14
EI481		600	1–3	12
EI612		600	1–3	15–25
EI765		700	10–13	20
EI826		800	4–7	14
EI827		800	2–6	18
EP220		900	2–3	10

Table 2: Influence of a long ageing time on the residual deformation
Tabela 2: Vpliv dolgega staranja na rezidualno deformacijo

Material	Temperature and time of preliminary aging		Stress, temperature and time to rupture in the creep test			Residual deformation (%)	
	T/°C	τ/h	σ/MPa	T/°C	τ_f/h	Momentary loading, ε_f	Creep, ε_c
EI787	–	–	350	650	8000	20	1,6
	650	50000	350	650	442	6	15,0
EP99	–	–	200	800	374	50.2	24
	800	5000	200	800	193	5.0	20.4
EP126	–	–	100	800	684	41	28,8
	800	5000	100	800	151	16	10.0
EI481	–	–	300	650	1000	23	4
	650	40000	300	650	72	20	30

4 INFLUENCE OF EXPOSURE TO HIGH TEMPERATURES ON THE DEFORMATION CAPACITY

Special experiments were carried out to determine the influence of preliminary aging without any load on the alloy microstructure and its resistance to deformation in the cases of momentary loading and in creep conditions[6] (**Table 2**). It was found that the microstructural changes caused by long-term aging affect differently the residual elongation after momentary deformation and after creep and, as shown in **Table 2**, on the deformation capacities ε_f and ε_c. Thus, the microstructure of the material is related to its mechanical state, which is a microstructural parameter.

Metallographic studies were also carried out during the deformation of samples of the alloy EI787 after aging for 50000 h at a temperature of 650 °C (state 2) in comparison with the initial state (state 1). For both states of material approximately equal values of yield stress (880 MPa and 900 MPa) were established with tensile tests (in the case of momentary loading). At the same time, the values of the plasticity and the time-to-rupture below 650 °C and a stress of 350 MPa were considerably different (**Table 3**).

Table 3: Influence of microstructure of the alloy EI787 on it deformation characteristics
Tabela 3: Vpliv stanja mikrostrukture zlitine EI787 na deformacijske značilnosti

Temperature of tests, T/°C	650		700	
State	1	2	1	2
Stress, σ/MPa	730–870	460–470	380–460	280–290
Number of grain borders where sliding is observed, (average), %	13.5	4.5	25	13.5
Share of deformation localized on the grain borders, %	3.3	0.5	8.2	1.6
Average value of inter-grain creeping, μm	0.098	0.018	0.326	0.072
Observed microcracks	2	0	10	0

The samples in these two states were deformed at a rate of 1 %/h until a total deformation of 1.9 % was accumulated at 650 °C and until 2.2 % deformation at 700 °C. The assessment of the microstructure in the axial and transverse directions has shown that (see **Table 3**):

- the aging processes decrease the deformation resistance for momentary loading of the alloy EI787;
- the aging process decreases the deformability of the alloy in the region of grain boundaries;
- the deformation capacity with short-term rupture is higher in the initial state than in the aged state, while during long-term rupture it is higher in the initial state than after ageing.

5 PHENOMENOLOGICAL DESCRIPTION OF THE CHARACTERISTICS OF THE MATERIAL

The described experimental data demonstrate that it is useful to expand the principle of development of the creep equation with the microstructural parameters of Rabotnov s_i, $i = 1...n$[3]

$$p^{\bullet} = F(s_1(\tau,T),s_2(\tau,T),s_3(\tau,T), ...T, \sigma) \quad (1)$$

for which the inclusion of other material characteristics:

$$\begin{aligned}
&\sigma_B = F(s_1(\tau,T),s_2(\tau,T),s_3(\tau,T), ...T, v)\\
&\sigma_{0,2} = F(s_1(\tau,T),s_2(\tau,T),s_3(\tau,T), ...T, v)\\
&\sigma_{lts} = F(s_1(\tau,T),s_2(\tau,T),s_3(\tau,T), ...T, \sigma)\\
&\delta = F(s_1(\tau,T),s_2(\tau,T),s_3(\tau,T),... T, v)\\
&\Delta\varepsilon = F(s_1(\tau,T),s_2(\tau,T),s_3(\tau,T),... T_{max}, T_{min}, N, \tau_c)\\
&S_{0,4} = F(s_1(\tau,T),s_2(\tau,T),s_3(\tau,T), ...T, v)\\
&dl/d\tau = F(s_1(\tau,T),s_2(\tau,T),s_3(\tau,T),... T, K_1)\\
&dl/dn = F(s_1(\tau,T),s_2(\tau,T),s_3(\tau,T),... T, K_1)
\end{aligned} \quad (2)$$

where v is the deformation rate, τ_c, T_{max}, T_{min}, N are the cycle period, the maximum and minimum cycle temperature, the number of cycles up to the fatigue crack's appearance during thermo-cyclic loading, and K_1 is the stress-intensity factor.

The problem was formulated[7] and the solution consisting of the determination of indices for the description of the state of the material's microstructure and its

physical relation to the parameters $s_1(\tau,T)$,$s_2(\tau,T)$,$s_3(\tau,T)$ was found with the Eqs (1) and (2).

For this reason, for the determination of the margins of safety for components operating at high temperature, it is useful to link the parameters of their strained and stressed state to the material characteristics of the actual microstructure.

Taking into account the different nature of momentary plastic deformation and creep deformation, it is preferable to use models of thermo-visco-elasto-plasticity, where irreversible deformations can be divided. In this case the accumulated damage was determined on the basis of the deformation criteria:

$$D = D_1 + D_2$$
$$D_1 = \varepsilon/\varepsilon_f,\ D_2 = p/\varepsilon_c \qquad (3)$$

Having accepted the described approaches to the estimation of the deformation mode and of safety factors, considering the changes in the material's microstructure, it is necessary to have data on the kinetics of change of the characteristics used for a strength calculation in the process of holding the material at high temperature for a long time: yield point $\sigma_{0.2}$, plasticity δ, creep rate $p^{\bullet}$, creep crack-growth rate dl/dτ, cyclic deformation resistance $S_{0.4}$, thermal fatigue resistance $\Delta\varepsilon$ and long-term strength σ_{lts}.

6 INTERFERENCE OF PROCESSES OF CREEP AND MOMENTARY DEFORMATION

For the case of the division of irreversible deformations as a measure of deformation damage to use in calculations, the equivalent irreversible deformation, defined in Eq. (4), can be used:

$$\varepsilon_{eq} = \varepsilon + p\varepsilon_f/\varepsilon_c \qquad (4)$$

In **Figure 3** the influence of creep deformation on the resistance to the momentary deformation of steel EI723 below 550 °C, is shown, which confirms the validity of the Eq.(4).

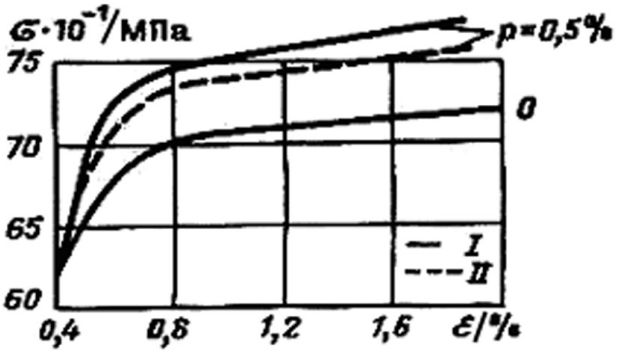

Figure 3: Influence of creep deformations on the resistance to momentary deformation of the steel EI723 at 550 °C, I —— experiment, II- - - - calculation

Slika 3: Vpliv deformacije z lezenjem na odpornost jekla EI 723 proti trenutni obremenitvi

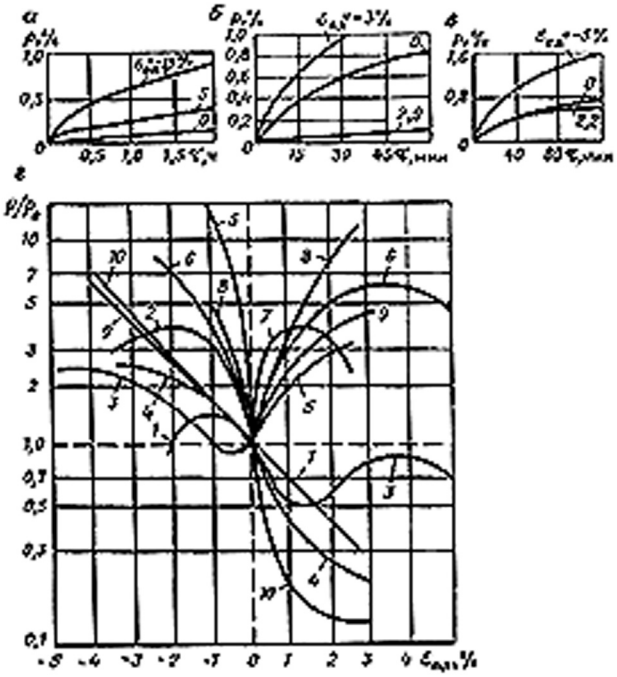

Figure 4: Dependence accumulated deformation related to the creep deformation after preliminary plastic deformation versus creep deformation in the initial state related to the value of the preliminary plastic deformation for different alloys and steels
a) EI765 at 750 °C; σ = 400 MPa, b) 20Ch23N18 at 750 °C, σ = 130 MPa, c) 15Ch12WNMV at 550 °C, σ = 320 MPa, d) 1-EI723 at 550 °C, σ = 550 MPa, τ = 1 h; 2-EI802 at 500 °C, σ = 400MPa, τ = 1 h; 3-EI802 at 550 °C, τ = 1 h, σ = 320 MPa; 4-20X23H18 at 750 °C, σ = 130 MPa, τ = 1 h; 5-EI765 at 750 °C, σ = 400 MPa, τ = 1 h; 6-EI765 at 700 °C, σ = 600 MPa, τ = 1 h; 7-EI698 at 700 °C, σ = 500 MPa, τ = 100 h; 8-EI698 at 750 °C, σ = 420 MPa, τ = 1 h; 9-EI607 at 650 °C, σ = 520 MPa, τ = 1 h; 10-20Ch23N18 at 800 °C, σ = 60 MPa, τ = 50 h
Slika 4: Razmerje akumulirana deformacija z lezenjem proti trenutni deformaciji v odvisnosti od razmerja deformacija z lezenjem proti predhodni plastični deformaciji za različne zlitine in jekla

The influence of momentary plastic deformation on the creep resistance depends on both the alloy composition and the direction of the preliminary deformation. In **Figure 4** the curves of the dependence of the accumulated creep deformation after preliminary plastic deformation related to the creep deformation in the initial state on the value of the preliminary plastic deformation at the same temperature are shown The experiments were carried out with ε varying from –5 % to +5 %. It was shown that even with a similar direction of deformation different alloys behave differently – some alloys get stronger and others become softer. In the case of a different direction of deformation, all the materials get stronger.

For the cyclic alternating deformation the character of the interference of creep deformation and momentary plastic deformation has specific features. A series of cyclic deformation tests was carried out for three levels of deformation amplitude with hard loading both in cyclic tension-pressure and in cyclic torsion. The values of the cyclic elastic limits were determined in cycles

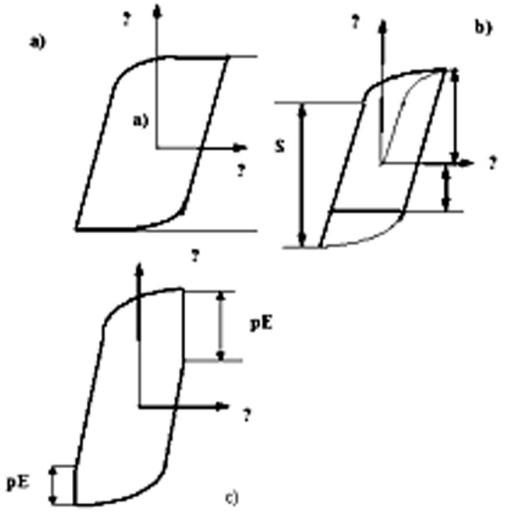

Figure 5: Cycles with the creep in bipolar semi-cycles (a,b) and in one semi-cycles (c)
Slika 5: Cikli z lezenjem v bipolarnih pol ciklih (a,b) in v eneme pol ciklu (c)

without creep, with creep in both semi-cycles, and with creep in one semi-cycle[8]. The creep deformation in the cycle did not exceed 1%. **Table 4** shows the values of the cyclic creep limit in relative units $\overline{S}_e^{(\kappa)} = S_e^{(\kappa)}/\sigma_e^{(0)}$, observed after the stabilization of the curves of cyclic deformation.

Table 4: Values of cyclic elasticity limit $\overline{S}_c^{(\kappa)}$
Tabela 4: Vrednosti ciklične meje elastičnosti $\overline{S}_c^{(\kappa)}$

Material	T/°C	$\overline{S}_c^{(\kappa)}$	
		Without creep	With creep in both semi-cycles
20Ch23N18	400	4.3	1.8
EI868	600	2.0–2.9	1.8
	700	2.5	1.8
EI765	700	1.9	1.4–1.7
EP220	900	1.9	1.3

The acceleration of creep from cycle to cycle is observed in case of cyclic deformation with creep in one semi-cycle (**Figure 5**). It was also found that the creep has a softening effect on the curve of cyclic deformation in the next semi-cycle: 1) the cyclic elastic limit decreases by the value $(S_{max}/2) - \sigma_{creep}$ (σ_{creep} – sample ageing stress); 2) during this aging partial annealing occurs, which lowers the cyclic strengthening. The analysis of experimental data has shown that the curves of deformation after creep on different levels may be described as central-like (curves with a constant relation in different points) with the similarity coefficient $\alpha_?$ in relation to the curve of deformation for the cycle without creep (with the same deformation amplitudes):

$$\alpha_c = A + B\,\sigma_{creep}/\sigma_c \qquad (5)$$

where A and B are temperature-dependent coefficients of the materials.

7 CONCLUSIONS

1. On the basis of results of experimental studies it was determined that the division of irreversible deformation into time-dependent and time-independent is necessary and expedient.
2. A general form of correlation was proposed for the description of the dependence of the material characteristics for the conditions of long-term exposure at high temperature.
3. Particularities of the interference of creep deformation and momentary deformation in conditions of static and cyclic deformation were established experimentally.
4. A method was proposed for the summing of the irreversible deformations, taking into account the difference in their nature.

8 REFERENCES

[1] Novozhilov, V., Kadashevich, Yu. Microstresses in engineering materials. Leningrad: Machine-building 1990, 223
[2] Perzyna, R.: Physical theory of viscoplasticity. Bull. Acad. Pol. Sci. Ser sci. Techn. 21 (**1973**) 3, 183–199
[3] Rabotnov, Yu. Creep in construction elements. M: Sci 1966, 752
[4] Rovinsky B. I., Liutsau V. G.: Relaxation of oriented microstresses. J. of Techn. Phys, 27 (**1957**) 2, 345–351
[5] Microplasticity (edited by Rakhshadt and Geminov). Moscow: Metallurgy 1972, 341
[6] Getsov, L. Materials and strength of gas turbine parts. 3rd ed. Moscow: Mines 1996, 591
[7] Getsov L. B., Rybnikov A. I., Pigrova G. D.: Change of steels and alloys structure and properties during long operation at high temperature. J. Phys IV France. 9(**1999**), 105–115
[8] Getsov, L., Gorsky, S., Kononov, K., Rebiakov, Yu.: Particularities of cyclic deformation of heat-resistant materials under high temperatures. Strength of materials. 7 (**1978**), 43–46

UDK 669.018.9:620.1./.2
Original scientific article/Izvirni znanstveni članek

ISSN 1580-2949
MTAEC9, 42(3)105(2008)

LOW-TEMPERATURE TRANSPORT PROPERTIES OF THE ε-PHASES Al-Pd-(Mn, Fe, Co, Rh)

NIZKOTEMPERATURNE TRANSPORTNE LASTNOSTI ε-FAZ Al-Pd-(Mn, Fe, Co, Rh, …)

Denis Stanić[1], Igor Smiljanić[1], Neven Barišić[1], Janez Dolinšek[2], Ante Bilušić[1,3], Jagoda Lukatela[1], Boran Leontić[1], Ana Smontara[1]

[1]Institute of Physics, Bijenička 46, HR-1000 Zagreb, Croatia
[2]J. Stefan Institute, Jamova 39, SI-1000 Ljubljana, Slovenia
[3]Faculty of Natural Sciences, University of Split, N. Tesle 12, HR-21000 Split, Croatia
dstanic@ifs.hr

Prejem rokopisa – received: 2007-07-12; sprejem za objavo – accepted for publication: 2007-12-14

We report results on low-tempertature investigations of the electrical and thermal conductivity of the ε-phases in the Al–Pd–Fe, Al–Pd–Co and Al–Pd–Rh systems, which are characterized by giant unit cells with a quasicrystals-like cluster substructure. The electrical resistivity is of the order of 100 μΩ cm and shows a weak temperature dependence in the investigated temperature interval 4–300 K. An interesting feature of the ε-phases is their low thermal conductivity, which at room temperature is comparable to that of thermally insulating amorphous SiO_2 and Zr/YO_2 ceramics. While SiO_2 and Zr/YO_2 are also electrical insulators, ε-phases exhibit an electrical conductivity typical of metallic alloys and offer an interesting combination of an electrical conductor and a thermal insulator. The reason for the weak thermal conductivity of the ε-phases appears to be structural: large and heavy atomic clusters of icosahedral symmetry in the giant unit cell prevent the propagation of extended phonons and the lattice can no more efficiently participate in the heat transport.

Keywords: complex intermetallic alloys; physical properties, resistivity, thermal conductivity

Predstavljamo nizkotemperaturne raziskave električne in toplotne prevodnosti ε-faz v sistemih Al-Pd-Fe, Al-Pd-Co in Al-Pd-Rh, ki jih karakterizirajo velike celice s podstrukturo iz klasterjev kvazikristalov. Električna upornost je reda velikosti 100 μΩ cm in je malo odvisna od temperature v preiskanem intervalu 4–300 K. Zanimiva značilnost ε-faz je njihova majhna toplotna prevodnost, ki je pri sobni temperaturi primerljiva tisti pri toplotnih izolatorjih amorfnemu SiO_2 in Zr/YO_2-keramiki, ki pa sta električna izolatorja. Nasprotno, ε-faze imajo električno prevodnost, ki je značilna za kovinske zlitine in dajejo zanimivo kombinacijo električnega prevodnika in toplotnega izolatorja. Vzrok za majhno toplotno prevodnost ε faz so verjetno strukturni, veliki in težki klasterji atomov z ikozaedrično simetrijo, ki v veliki celici preprečujejo propagacijo razširjenih fononov, zato mreža ne more sodelovati učinkovito pri transportu toplote.

Ključne besede: kompleksne intermetalne zlitine, fizikalne lastnosti, upornost, toplotna prevodnost

1 INTRODUCTION

Among the complex metallic alloys (CMAs), an interesting family of related structures is found in the Al–Pd [1] and Al–Rh [2] alloys systems and their ternaries Al-Pd-(Mn, Fe, Co, Rh, etc.) with transition metals [3–8]. These so-called ε-phases have been observed in wide compositional ranges and, depending on their composition, contain a row of giant-unit-cell orthorhombic structures and aperiodic structures in one dimension [7]. In the recent studies of Al–Pd–Fe [5], Al–Pd–Co [6] and Al–Pd–Rh [8] phase diagrams, the concentration ranges of the ε-phases were determined for different temperatures and large samples were grown. Here we present a study of their electrical and thermal properties and show that ε-phases offer a promising combination of a metallic electrical conductor with a thermal insulator. In our recent investigation[9], the physical properties of e-phases were determined in $Al_{74}Pd_{22}Mn_4$. The present work extends the exploration of these properties to a wide assortment of components, compositions and structural variants of the e-phases.

2 EXPERIMENTAL

The Al–Pd–Fe, Al–Pd–Co and Al–Pd–Rh samples investigated were polycrystalline materials, produced by levitation induction melting in a water-cooled copper crucible, as described in detail elsewhere [5,6,8]. Parts of the ingots were annealed under argon or vacuum for up to 2 441 h and then water-quenched. The structural characterization was performed by powder X-ray diffraction and scanning electron microscopy, which showed that the selected samples were pure materials, not contaminated by secondary phases. Four Al–Pd–Fe, two Al–Pd–Co, two Al–Pd–Rh and an Al–Rh sample were included in the study. Their nominal compositions and electrical resistivity data ($\rho_{300\,K}$ and the ratio ($\rho_{300\,K}/\rho_{4K}$) are given in **Table 1**. In the following we abbreviate their compositions by the symbols of their constituent elements and the number denoting the concentration (in %) of the transition element (e. g., the sample $Al_{74}Pd_{12.5}Co_{13.5}$ is abbreviated as $AlPdCo_{13.5}$).

In order to measure the electrical and thermal conductivity of a given material, a specimen in the form

Table 1: The nominal composition and the electrical resistivity data for the investigated samples
Tabela 1: Nazivna sestava in podatki o električni upornosti preiskanih vzorcev

Number	Composition	Abbre-viation	ρ_{300K}/(μΩ cm)	ρ_{300K}/ρ_{4K}
1	$Al_{73}Pd_{25}Fe_2$	$AlPdFe_2$	112	2,02
2	$Al_{71}Pd_{24}Fe_5$	$AlPdFe_5$	270	1,18
3	$Al_{73}Pd_{20}Fe_7$	$AlPdFe_7$	586	1,03
4	$Al_{75.5}Pd_{14.5}Fe_{10}$	$AlPdFe_{10}$	376	1,02
5	$Al_{74}Pd_{12.5}Co_{13.5}$	$AlPdCo_{13.5}$	260	1,52
6	$Al_{73.5}Pd_{11}Co_{15.5}$	$AlPdCo_{15.5}$	438	1,04
7	$Al_{74}Pd_{15}Rh_{11}$	$AlPdh_{11}$	579	1,02
8	$Al_{74.5}Pd_9Rh_{16.5}$	$AlPdRh_{16.5}$	308	1,19
9	$Al_{76}Rh_{24}$	$AlRh_{24}$	1212	0,97

of a bar with dimensions ≈ (1.9 x 0.5 x 0.5) mm was cut from the ingot. The sample faces were then polished using emery paper. The sample was cooled using a ^{4}He flux cryostat between 4 K and 300 K. The electrical resistivity was measured by a four-probe low-frequency ac-method, whereas for the measurement of the thermal conductivity a standard steady-state heat-flow technique was used. For thermal conductivity measurements, one end the bar-shaped sample was glued to a heat sink made of copper by means of GE varnish. The sample heater, attached to the other end with the same glue, consisted of a 100-V ruthenium-oxide chip resistor. With the aim to measure the thermal gradient along the sample we used calibrated chromel-gold/iron thermocouples. Very thin, 25 μm in diameter, and up to 10 cm long, wires were chosen in order to reduce the heat flow through the thermocouples. The temperature difference of the sample was always kept smaller than 1K. The cooling (heating) rate was generally 5 K/h or less. Thermal conductivity measurements of materials with low thermal conductivity values are generally difficult to perform at high temperatures because of the detrimental effect of radiative losses on the results. In order to limit this type of energy dissipation, a cylindrical radiation shield in good thermal contact with the heat sink was used. With this setup, the radiative losses in our measurements were estimated to be below 1 % of the applied power over the whole temperature range and the relative accuracy of the measurement (1–2 %) was much better than that for the absolute values. Considering the length of the samples and the lateral extension of the thermal contacts, the uncertainty in the geometrical factor was estimated to be about 10–20 %, where the larger errors correspond to the shorter samples. We used the same sample geometry for both the electrical resistivity and thermal conductivity measurements in order to avoid additional uncertainties that could arise in the subtraction of the electronic contribution to the measured thermal conductivity.

3 RESULTS AND ANALYSIS

3.1 Electrical resistivity

The resistivity of all the samples is shown in **Figure 1**. The room temperature resistivity of most samples is in the range 200–600 μΩ cm and exhibits small temperature variations of a few percentages between 300 K and 4 K. Exceptions are the samples $AlPdFe_2$, with lower resistivities ($\rho_{300\ K}$ = 112 μΩ cm and $\rho_{300\ K}/\rho_{4\ K}$ = 2.02), and $AlRh_{24}$, with the highest resistivity ($\rho_{300\ K}$ = 1212 μΩ cm). The $AlRh_{24}$ sample also exhibits a small negative temperature coefficient ($\rho_{300\ K}/\rho_{4\ K}$ = 0.97), in contrast to all the other samples, which show positive temperature coefficients. The above resistivity (of polygrain samples) compares well to the resistivity of monocrystalline ε-phase Al–Pd–Mn, which amounts to $\rho_{300\ K} \approx 200$ μΩ cm [9] and exhibits a practically zero temperature coefficient ($\rho_{300\ K}/\rho_{4\ K} \approx 1.01$). An interesting feature, related to the weak Curie paramagnetism detected recently in the samples [10], is also observed in the $\rho(T)$ curves. In **Figure 2**, we show the resistivity of the three Al–Pd–Fe samples with the highest Fe content (i.e. $AlPdFe_{10}$, $AlPdFe_7$ and $AlPdFe_5$) on a $\rho/\rho_{300\ K}$ normalized scale. The resistivity exhibits a small, positive temperature coefficient, indicating that phonons play a role in the temperature dependence of $\rho(T)$. At

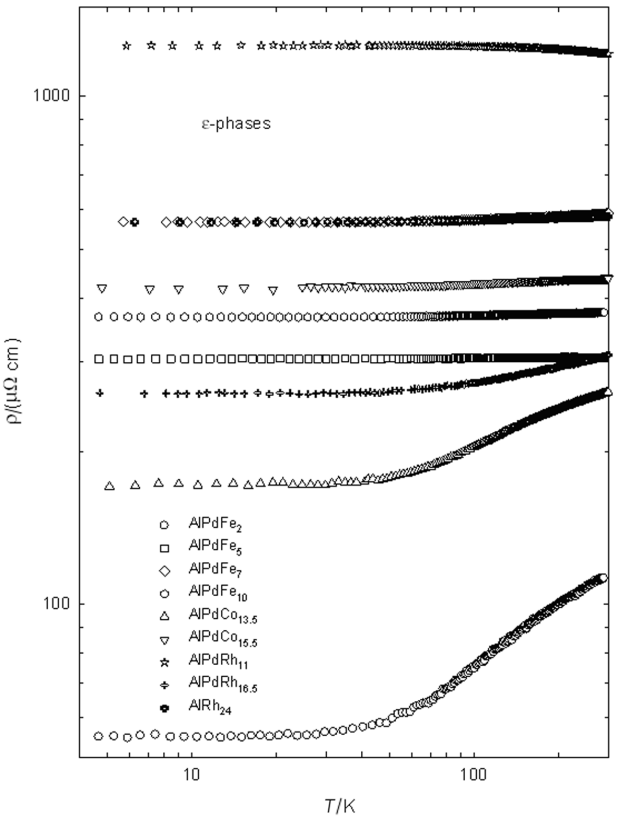

Figure 1: The electrical resistivity ρ (T) of the ε-phase samples in the Al–Pd–Fe, Al–Pd–Co and Al–Pd–Rh systems
Slika 1: Električna prevodnost $\rho(T)$ za ε faze v sistemih Al-Pd-Fe, Al-PdCo in Al-Pd-Rh

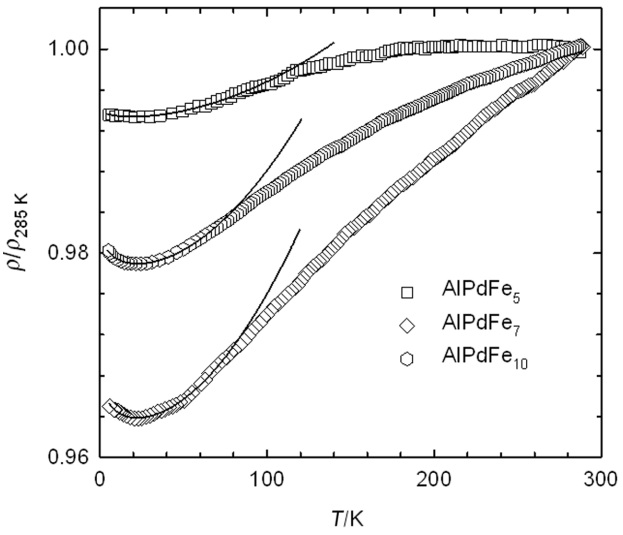

Figure 2: The electrical resistivity of the three Al–Pd–Fe samples with the highest Fe content on a $\rho/\rho_{300\ K}$ normalized scale.
Slika 2: Električna upornost treh vzorcev Al-Pd-Fe z največjo vsebnostjo Fe na ρ/ρ_{300} normalizirani skali

low temperatures, the resistivity exhibits a minimum that is most pronounced for the $AlPdFe_{10}$ sample. It is still clearly recognizable for the $AlPdFe_7$ and becomes less obvious for the $AlPdFe_5$. According to magnetic measurements [10], it is reasonable to assume that Al–Pd–Fe samples with a higher Fe content are more magnetic. For the $AlPdFe_5$ sample it was estimated that a fraction of 0.00041 of all the Fe atoms in the sample carry localized magnetic moments [10]. It is known that a small amount of transition-metal impurities of this order of magnitude dissolved in a metal introduce a minimum in the $\rho(T)$ (e.g., in Cu metal with 0.00044 Fe, the minimum was observed at 25 K [12]). The reason is the s–d exchange interaction between the s-moments of the conduction electrons and the d-moments of the transition–metal impurities, which contributes to the resistivity [11]. The total resistivity at low temperatures can be expressed as a sum of the electron–phonon contribution (e.g., by the Bloch–Grüneisen contribution $\rho = \rho_0 + bT^5$ for regular metals, or by its modification $\rho = \rho_0 + bT^2$ in the case of amorphous alloys [13], to which ε-phases show certain resemblance on the interatomic scale due to an icosahedral near-neighbor coordination that is characteristic of the amorphous alloys as well [14]) and the s–d contribution:

$$\rho = a + bT^2 + d \lg T \qquad (1)$$

where *a, b* and *d* are fitting parameters. Using this expression, one can fit well the experimental data up to 70 K, but fits should be considered as qualitative due to the limited temperature range of the analysis. The shift of the resistivity minimum to lower temperatures for samples with a lower Fe concentration is consistently observed, in agreement with the prediction of the expression.

Also of general interest, in the context of giant-unit-cell complex metallic alloys, is the question which of the two coexisting physical length scales – the large-scale periodicity versus the atomic-scale icosahedral order – plays the dominant role in determining the electrical transport properties of the complex metallic alloys. This question can be addressed by applying pressure to the sample in an electrical resistivity experiment. Pressure-induced compression of the lattice brings the atoms closer together, so that the overlap of the atomic potentials is larger and the potential barriers between neighboring atoms are reduced, which should enhance the electronic transport. The application of pressure should thus change the electrical resistivity due to atomic-scale effects. Indeed, preliminary measurements show that the resistivity of ε-$Al_{75}Pd_{20}Fe_5$ drops significantly with pressure from $\rho_{300\ K}$(0 bar) = 306 μΩ cm to $\rho_{300\ K}$(17.8 kbar) = 284 μΩ cm, thus by 7 % relative to the $p = 0$ value, whereas this reduction amounts 8.5 % at 4 K [10]. This behavior is consistent with the consideration that the resistivity of a complex metallic material is governed by the smaller of the two coexisting physical length scales – that of the interatomic distances – whereas the large-scale periodicity is of marginal importance for the electronic transport.

3.2 Thermal conductivity

The measured thermal conductivities $\kappa(T)$ of all the samples are displayed in **Figure 3** on a lg–lg scale. The surprising results are the low $\kappa(T)$ values, which are in the range $\kappa_{300\ K} \approx 2$–10 W/mK at room temperature. The conductivities of the $AlRh_{24}$ and $AlPdRh_{11}$ samples are even as low as $\kappa_{300\ K} = 2$ W/mK. These $\kappa_{300\ K}$ values, very low for alloys of regular metals, are comparable to the thermal conductivity of amorphous SiO_2 ($\kappa_{300\ K} = 2.8$ W/mK), a known electrical and thermal insulator, as well as to the technologically widespread thermally insulating material yttrium-doped zirconia ceramics $Zr_{1-x}Y_xO_{2-x/2}$ ($x < 0.2$), where $\kappa_{300\ K} \approx 2$ W/mK [21]. The thermal conductivity model appropriate to complex metallic alloys with the large-scale periodicity of the lattice and the small-scale atomic clustering structure has been described in detail in the previous investigation of ε-phases in the Al–Pd–Mn system [9] as well as of the giant-unit-cell orthorhombic phases in the Al–Cr–Fe system [15] and the "Bergman phase" $Mg_{32}(Al,Zn)_{49}$ [16]. The total thermal conductivity parameter $\kappa(T)$ is divided into three terms:

$$\kappa(T) = \kappa_{el}(T) + \kappa_D(T) + \kappa_H(T) \qquad (2)$$

The electronic contribution κ_{el} is estimated from the measured electrical resistivity data using the Wiedemann–Franz law, $\kappa_{el} = L_0T/\rho$, where L_0 is the Lorenz number. The lattice contribution $\kappa_l = \kappa - \kappa_{el}$ is analysed by considering the propagation of long-wavelength phonons within the Debye model and the hopping of localized vibrations. This picture assumes that large

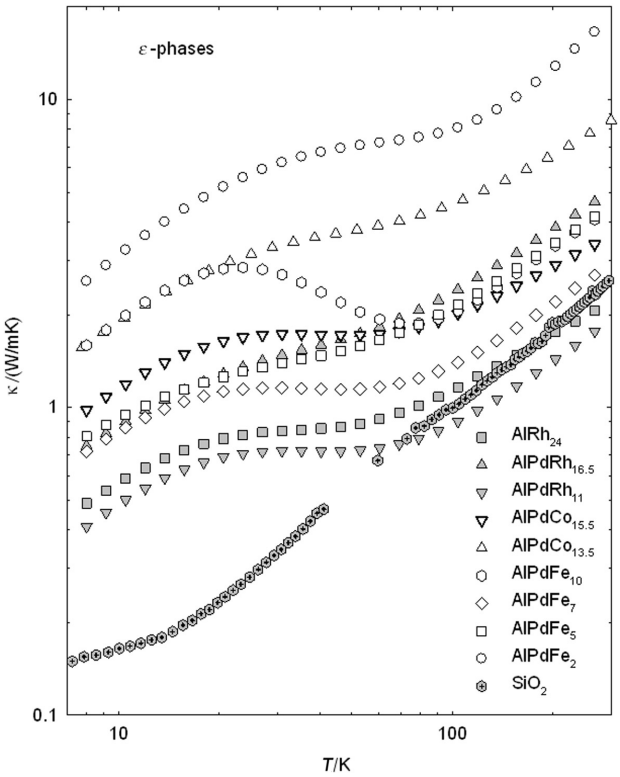

Figure 3: The thermal conductivities $\kappa(T)$ of the ε-phase samples between 8 K and 300 K. The thermal conductivity of amorphous SiO_2 is shown for comparison.

Slika 3: Toplotna prevodnost $\kappa(T)$ vzorcev ε-faz med 8 K in 300 K. Toplotna prevodnost amorfnega SiO_2 je prikazana za primarjavo

atomic clusters of icosahedral symmetry strongly suppress the propagation of phonons in the lattice of complex metallic alloys. The exceptions are long-wavelength acoustic phonons, for which this material is an elastic continuum, and fracton-like localized vibrations within the cluster substructure that can participate in the heat transfer via thermally activated hopping. In the simplest model, the hopping of localized vibrations is described by a single activation energy E_a, yielding a contribution to the thermal conductivity $\kappa_H = \kappa_H{}^0 \exp(-E_a/k_BT)$, where $\kappa_H{}^0$ is a constant. The Debye thermal conductivity is written as:

$$\kappa_D = C_D T^3 \int_0^{\theta_D/T} \tau(x) \frac{x^4 e^x}{(e^x - 1)^2} \mathrm{d}x \qquad (3)$$

where $C_D = k_B{}^4/2\pi^2\bar{v}\hbar^3$, $\bar{v}$ is the average sound velocity, θ_D is the Debye temperature, τ is the phonon relaxation time and $x = \hbar\omega/k_BT$, where $\hbar\omega$ is the phonon energy. The different phonon-scattering processes are incorporated into the relaxation time $\tau(x)$ and we assume that Matthiessen's rule is valid, $\tau^{-1} = \Sigma\tau_j^{-1}$, where τ_j^{-1} is a scattering rate related to the j-th scattering channel. In analogy to the ε-phases in Al–Pd–Mn [9], we consider two dominant scattering processes in the investigated temperature interval (from 8 K to 300 K): (1) the scattering of phonons on structural defects of the stacking-fault type with the scattering rate $\tau_{sf}^{-1} = Ax^2T^2$ and (2) *umklapp* processes with the phenomenological form of the scattering rate pertinent to complex metallic alloys [9,15], $\tau_{um}^{-1} = Bx^{\alpha}T^{\beta}$, so that $\tau^{-1} = \tau_{sf}^{-1} + \tau_{um}^{-1}$. The Debye temperature of the investigated ε-phases is not known, therefore we have used the θ_D value reported for the related icosahedral *i*-Al–Pd–Mn quasicrystals, where θ_D was commonly found to be close to 500 K [18,19]. Since our $\kappa(T)$ data are available only up to 300 K, it turns out that the fit is insensitive to a slight change of this θ_D value, so that a fixed θ_D = 500 *K* is used. The Debye constant C_D was also not taken as a free

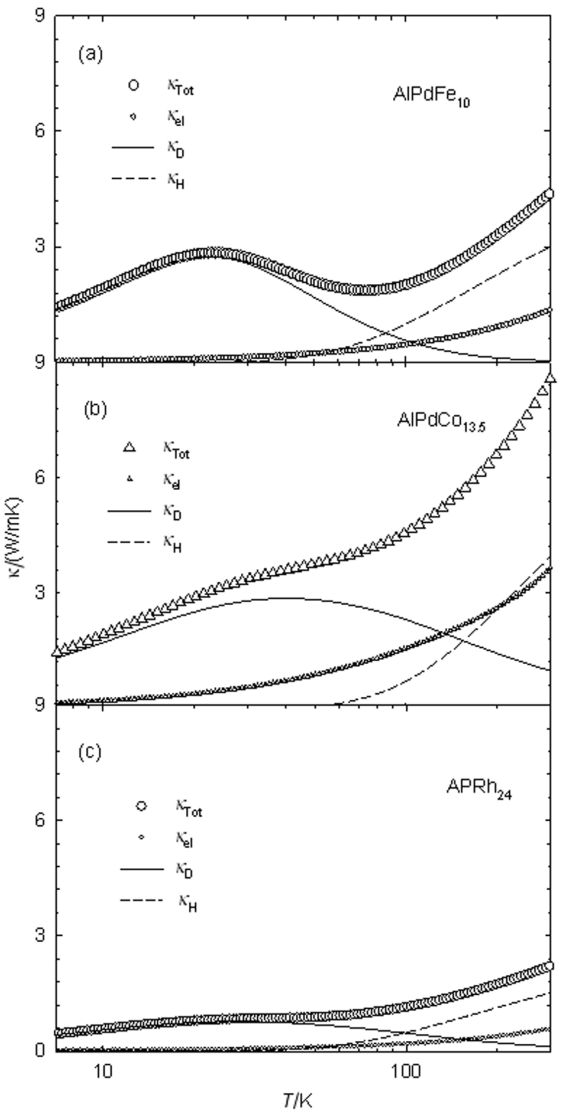

Figure 4: Thermal conductivities $\kappa(T)$ of the $AlPdFe_{10}$ **(a)**, $AlPdCo_{13.5}$ **(b)** and $AlPdRh_{24}$ **(c).** The three contributions to the total $\kappa(T)$ – large symbols, obtained using **Eq. (2)** are shown separately. The electronic contribution κ_{el}-small symbols, the Debye contribution κ_D – solid line and the hopping contribution κ_H – dashed line.

Slika 4: Toplotne prevodnosti $\kappa(T)$ za $AlPdFe_{10}$ (a), $AlPdCo_{13}$ (b) in $AlPdRh_{24}$ (c). Trije deli celotne $\kappa(T)$ – veliki simboli, dobljeni z uporabo enačbe (2), so prikazani ločeno. Elektronski delež κ_{el} – majhni simboli, Debyev delež κ_D – cela črta in hopping delež κ_H – črtkana črta.

Table 2: Fit parameters of the thermal conductivities $\kappa(T)$ from **Figure 3**
Tabela 2: "Fit"-parametri za toplotno prevodnost $\kappa(T)$ iz **slike 3**

Sample	A ($\times 10^6$ s^{-1} K^{-2})	B ($\times 10^4$ s^{-1})	α	β	κ_H° (W/mK)	E_a (K)
$AlPdFe_2$	4.2	1.5	2.0	3.6	37.2	373
$AlPdFe_5$	11.3	11.4	2.2	3.5	3.0	215
$AlPdFe_7$	12.5	5.2	1.3	3.9	2.8	174
$AlPdFe_{10}$	6.3	0.14	1.6	4.6	5.2	166
$AlPdCo_{13.5}$	6.1	2.9	2.5	3.6	9.4	259
$AlPdCo_{15.5}$	9.4	3.7	2.0	3.8	5.0	183
$AlPdRh_{11}$	24.6	38.1	2.4	4.0	1.0	176
$AlPdRh_{16.5}$	12.0	18.3	2.1	3.4	4.7	238
$AlRh_{24}$	18.4	11.0	2.0	3.7	2.7	171

parameter, but was instead calculated by using $\bar{v}$ = 4 004 ms^{-1}, a value determined for the *i*-Al–Pd–Mn from ultrasonic data [20]. The thermal conductivities of the ε-phase samples were analysed by means of **Eq. (2)**. The total $\kappa(T)$'s were resolved into the electronic (κ_{el}), Debye (κ_D) and hopping (κ_H) contributions, which are shown separately on the graphs. The $\kappa(T)$'s of the Al–Pd–Fe sample are shown in **Figure 4a**, that of Al–Pd–Co in **Figure 4b**, and that of Al–Pd–Rh in **Figure 4c**, whereas the fit parameters are collected in **Table 2,** together with the fit parameters obtained for all the investigated samples. A common characteristic of all the ε-phase samples is a small Debye contribution (its maximum value is in the range $\kappa_{D,max} \approx$ 0.5–4 W/mK) and a significant hopping contribution at elevated temperatures. A qualitative explanation of this result is that large atomic clusters of icosahedral symmetry suppress the heat transfer by phonons, whereas localized cluster vibrations still provide a weak lattice heat-conduction channel. In addition, conduction electrons contribute the usual channel to the heat conductivity, but since the electrical resistivity of the ε-phase is of few 100 μΩ cm, the electronic thermal conductivity contribution is also not large. Consequently, the total thermal conductivities of the ε-phase materials are about the same as that of amorphous SiO_2. Here it is important to point out that while SiO_2 is both a thermal and an electrical insulator, the ε-phase complex metallic alloys offer a combination of a thermal insulator with an electrical conductor, which can be considered as a "smart" property of the material, not realized in conventional solid-state materials. Here we also stress that our thermal conductivity values, obtained on polygrain materials, are practically the same as those obtained on ε-phase Al–Pd–Mn monocrystalline samples [9]. Thus, polycrystallinity does not have a significant influence on the thermal response of the ε-phase material. The cluster substructure very likely already provides enough phonon scattering centers to suppress the phonon propagation, so that additional scattering at the grain boundaries does not add much to this effect. A similar consideration also seems to hold for the electron scattering in the electronic transport. The thermal conductivity fit parameters in **Table 2** allow us to derive some average properties of the ε-phases. The average hopping activation energy of the localized vibrations is $\bar{E}_a$ = 209 ± 49 K (or (18 ± 4) meV), which is similar to the values observed in *i*-Al–Pd–Mn QCs [9]. The average values of the exponents α and β that govern the frequency and temperature dependencies of the *umklapp* rate are $\bar{\alpha}$ = 2.0 ± 0.4 and $\bar{\beta}$ = 3.8 ± 0.8, yielding the average dependence $\tau_{um}^{-1} \propto \omega^2 T^{1.8}$. This is close to the phenomenological power-law $\omega^2 T^2$, sometimes observed in systems with a dense distribution of energy gaps in the vibrational spectrum, like in icosahedral Al-based quasicrystals. Very small thermal conductivities, κ < 4.5 W/mK in the temperature interval 2–300 K, were reported recently [27] also for a series of related complex metallic materials, the Al-based Mackay-type 1/1 cubic approximants. In contrast to our phenomenological analysis of the thermal conductivity, the explanation of the anomalously low thermal conductivity in [28] was derived from first-principle calculations of the phonon dispersion, using crystallographic structure data of the investigated materials. It was found that the combination of a small group velocity and the large number of optical phonon branches caused by the large number of atoms in the unit cell greatly reduces the lattice thermal conductivity by increasing the probability of the *umklapp* processes in the phonon scattering. The presence of vacancies in the structure further enhances this tendency. We expect that a similar microscopic picture also explains the anomalously low thermal conductivity of the ε-phases. There is one marked difference in the thermal conductivities of the ε-phases and the approximants studied in [28]. While the thermal conductivities of the latter materials exhibit a very weak temperature dependence above 100 K (see **Figure 2** of [28]), our ε-phase materials exhibit an exponential increase above about 70 K (**Figure 4**), which we model phenomenologically with a thermally activated behavior using an activation energy E_a and attribute it to the hopping of localized vibrations (i.e., a given locally-vibrating atomic cluster "hits" its neighbor).

4 CONCLUSIONS

The electrical resistivity of the ε-phases is moderate, in the range of a few 100 μΩ cm, and shows a weak temperature dependence (in most cases of a few percentages) in the investigated temperature interval 4–300 K. An interesting feature of the ε-phases is their low thermal conductivity, which at room temperature is about the same as that of known thermal insulators like amorphous SiO_2 and Zr/YO_2 ceramics. While SiO_2 and Zr/YO_2 are also electrical insulators, the ε-phases exhibit an electrical conductivity typical of metallic alloys, so

that this material offers an interesting combination of an electrical conductor together with a thermal insulator. The reason for the weak heat conductivity of the ε-phases appears to be structural: large and heavy atomic clusters of icosahedral symmetry in the giant unit cell suppress the propagation of extended phonons, so that the lattice cannot efficiently participate in the heat transport (apart from the remaining weak channel of the hopping of localized vibrations). As the cluster substructure is a common feature of complex metallic alloys, a low thermal conductivity at a moderate electrical conductivity can be expected to be a general property of this class of materials. The ε-phase material can thus be considered as a promising candidate for the development of a technologically interesting "smart" material that combines the properties of an electrical conductor with a thermal insulator.

Acknowledgements

We would like to thank Mr. B. Grushko for giving us the samples and for stimulating discussions. This work was done within the activities of the EU Network of Excellence "Complex Metallic Alloys" (Contract No. NMP3-CT-2005-500140), and has been supported in part by the Ministry of Science, Education and Sports of Republic of Croatia through the Research Projects No. 035-0352826-2848 and 177-0352828-0478.

5 REFERENCES

[1] M. Yurechko, A. Fattah, T. Velikanova, B. Grushko, J. Alloys Compd. 329 (**2001**), 173–181

[2] B. Grushko, J. Gwóźdź, M. Yurechko, J. Alloys Compd. 305 (**2000**), 219–224

[3] M. Boudard, H. Klein, M. de Boissieu, M. Audier, H. Vincent, Philos. Mag. A 74 (**1996**), 939–956

[4] H. Klein, M. Audier, M. Boudard, M. de Boissieu, L. Beraha and M. Duneau, Philos. Mag. A 73 (**1996**), 309–331

[5] S. Balanetskyy, B. Grushko, T.Ya. Velikanova, K. Urban, J. Alloys Compd. 376 (**2004**), 158–164

[6] M. Yurechko, B. Grushko, T. Velikanova, K. Urban, J. Alloys Compd. 337 (**2002**), 172–181

[7] S. Balanetskyy, B. Grushko, T. Ya. Velikanova, Z. Kristall. 219 (**2004**), 548–553

[8] B. Przepiórzynski, B. Grushko, M. Surowiec, Intermetallics 14 (**2006**), 498–504

[9] J. Dolinšek, P. Jeglič, P. J. McGuiness, Z. Jagličić, A. Bilušić, Ž. Bihar, A. Smontara, C. V. Landauro, M. Feuerbacher, B. Grushko, K. Urban, Phys. Rev. B 72 (**2005**), 064208-1–11

[10] A. Smontara, I. Smiljanić, A. Bilušić, B. Grushko, S. Balanetskyy, Z. Jagličić, S. Vrtnik, J. Dolinšek, J. Alloys Compd. 450 (**2008**) 92–102

[11] See, e.g.: U. Mizutani, Electron Theory of Metals, Cambridge University Press (2001), p. 416

[12] J. M. Ziman, Electrons and Phonons, Clarendon Press, Oxford (1962), 244

[13] U. Mizutani, Electron Theory of Metals, Cambridge University Press (2001), 480

[14] W. K. Luo, H. W. Sheng, F. M. Alamgir, J. M. Bai, J. H. He, E. Ma, Phys. Rev. Lett. 92 (**2004**), 145502–145505

[15] Ž. Bihar, A. Bilušić, J. Lukatela, A. Smontara, P. Jeglič, P. J. McGuiness, J. Dolinšek, Z. Jagličić, J. Janovec, V. Demange, J. M. Dubois, J. Alloys Compd. 407 (**2006**), 65–73

[16] A. Smontara, I. Smiljanić, A. Bilušić, Z. Jagličić, M. Klanjšek, S. Roitsch, J. Dolinšek, M. Feuerbacher, J. Alloys Compd. 439 (**2007**), 29–38

[17] R. Berman, Thermal Conduction in Solids, Oxford University Press (1978), 23

[18] A. Bilušić, A. Smontara, J. Dolinšek, P.J. McGuiness, H.R. Ott, J. Alloys Compd. 432 (**2007**), 1–6

[19] C. Wälti, E. Felder, M. A. Chernikov, H. R. Ott, M. de Boissieu, C. Janot, Phys. Rev. B 57 (**1998**), 10504–10511

[20] Y. Amazit, M. de Boissieu, A. Zarembowitch, Europhys. Lett. 20 (**1992**), 703–706

[21] R. Mévrel, J.-C. Laizet, A. Azzopardi, B. Leclercq, M. Poulain, O. Lavigne, D. Demange, J. Eur. Ceram. Soc. 24 (**2004**), 3081–3089

[22] C. Janot, A. Magerl, B. Frick, M. de Boissieu, Phys. Rev. Lett. 71 (**1993**), 871–874

[23] M. de Boissieu, M. Boudard, R. Bellissent, M. Quilichini, B. Henion, R. Currat, A.I. Goldman, C. Janot, J. Phys.: Condens. Matter. 5 (**1993**), 4945–4966

[24] M. Boudard, M. de Boissieu, S. Kycia, A. I. Goldman, B. Hennion, R. Bellissent, M. Quilichini, R. Currat, C. Janot, J. Phys.: Condens. Matter. 7 (**1995**), 7299–7308

[25] M. Krisch, R. A. Brand, M.A. Chernikov, H. R. Ott, Phys. Rev. B 65 (**2002**), 134201-1–8

[26] T. Takeuchi, N. Nagasako, R. Asahi, U. Mizutani, Phys. Rev. B 74 (**2006**), 054206-1–12

[27] N. F. Mott, H. A. Jones, The Theory of the Properties of Metals and Alloys, Clarendon, Oxford 1936, 23

UDK 669.71:620.1./.2
Original scientific article/Izvirni znanstveni članek

ISSN 1580-2949
MTAEC9, 42(3)111(2008)

THE ACTION OF A LASER ON AN ALUMINIUM TARGET

OBSEVANJE ALUMINIJASTE TARČE Z LASERJEM

Višnja Henč-Bartolić[1], Tonica Bončina[2], Suzana Jakovljević[3], Davor Pipić[1], Franc Zupanič[2]

[1]Faculty of Electrical Engineering and Computing, University of Zagreb, Unska 3, 10000 Zagreb, Croatia
[2]Faculty of Mechanical Engineering, University of Maribor, Smetanova 17, 2000 Maribor, Slovenia
[3]Faculty of Mechanical Engineering and Naval Architecture, University of Zagreb, I. Lučića 1, 10000 Zagreb, Croatia
visnja.henc@fer.hr

Prejem rokopisa – received: 2007-08-08; sprejem za objavo – accepted for publication: 2008-02-05

A nitrogen laser beam (337 nm, 6 ns (FWHM), (3.2 ± 0.2) mJ) was focused with a quartz lens (f = 100 mm) onto an aluminium target in air at normal pressure. The laser irradiation and plasma explosion caused a modification to the Al surface and the deposition of a thin film (droplets) onto a glassy carbon plate. The irradiated target and the deposited material were studied with a scanning electron microscope (SEM) and a focused-ion-beam (FIB) device. A crater surrounded by a rim was produced on the spot of maximum irradiation on the aluminium target. The crater, very deep in comparison to its width and thickness, was presumably caused by the Kelvin-Helmholtz and the Rayleigh-Taylor instabilities. The temperatures of the electron and the massive particles were explained.

Key words: aluminium, laser ablation, thin film deposition, instabilities, temperatures

Žarek laserske svetlobe (337 nm, 6 ns ((FWHM), (3.2 ± 0.2) mJ) smo s kremenovo lečo (f = 100 mm) fokusirali na aluminijevo tarčo, ki je bila na zraku pri normalnem zračnem tlaku. Obsevanje z laserjem in eksplozija plazme sta povzročila spremembo površine aluminija ter nanos tanke plasti in kapljic na steklasto ogljikovo ploščico. Obsevano tarčo in nanesen material smo raziskali z vrstičnim elektronskim mikroskopom (SEM) in s fokusiranim ionskim curkom (FIB). Na aluminijevi tarči je na najbolj obsevanem mestu nastal krater, ki je bil zelo globok v primerjavi z njegovo širino in debelino. Krater bil povzročen zaradi Kelvin-Helmholtzove in Rayleigh-Taylorjeve nestabilnosti. V delu smo razložili tudi temperaturo elektronov in temperaturo masivnih delcev.

Ključne besede: aluminij, laserska ablacija, nanašanje tanke plasti, nestabilnosti, temperatura

1 INTRODUCTION

The laser irradiation of a target has wide applications; some examples include pulsed-laser deposition [1,2], nanoparticle manufacturing [3], and the analysis of solid materials [4,5]. It is important to reduce the plume's kinetic energy by means of a buffer gas [6] to attain a better quality of the deposited film. In this experiment we used the pulsed-laser deposition of Al droplets in air at normal pressure. It is known that the laser's interaction with matter causes melting and evaporation of the target material. Additionally, laser beams ionize the material when the power flux is sufficiently high (>1 MW/cm^2). The result is the creation of a plasma plume near the target surface. The aim of this research was to study the irradiated aluminium surface and the plasma deposit on the glassy carbon plate.

2 EXPERIMENTAL SET-UP

In the present experiment we used a pure (99.9 %) Al specimen as the target, which was irradiated with a nitrogen laser emitting pulses of 6-ns duration with an average pulse energy of (3.2 ± 0.2) mJ and a wavelength of 377 nm. The laser caused a major modification to the target surface, characteristic for these types of devices. The laser radiation was focused with a quartz lens (f = 100 mm) perpendicularly onto the aluminium target surface that was placed in air at normal pressure (**Figure 1**). The modified surface, i.e., the crater, where the irradiation and laser ablation were a maximum, was examined with a scanning electron microscope (SEM) and with a focused-ion-beam (FIB) device. The emitted plumes, a consequence of the laser ablation, were laterally deposited on the glassy carbon plate (**Figure 1**) and analyzed with the SEM.

2.1 Characteristics of the Al target

An aluminium sample of 1 cm × 1 cm × 0.3 cm was mechanically polished and cleaned with an ultrasonic device. The purity of the sample was 99.9 %. Before the laser-beam irradiation, the subsurface microstructure of the target was observed (**Figure 2**) by means of a FIB device. The small black dots (diameter ≈ 100 nm) could be explained in terms of pores. Also, the EDS analysis (**Table 1**) shows the areas of the intermetallic phases (B_1, B_2 on **Figure 2**) between Al, Fe and Si. Both appearances made stronger, deeper damage to the target during the irradiation with the laser beam. Otherwise, the UV nitrogen laser beam is absorbed in a very shallow region near the irradiated spot. The subsurface area of the Al sample was deformed due to machining. How-

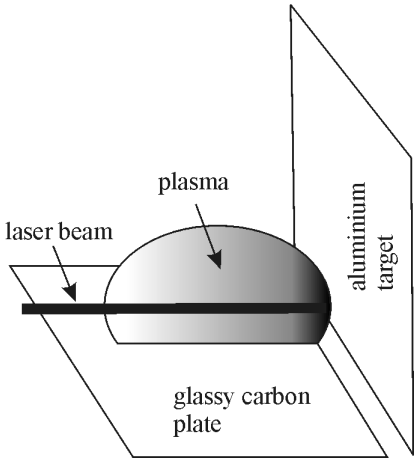

Figure 1: Target position. Relative position of Al target, carbon plate and laser beam
Slika 1: Položaj tarče. Relativen položaj aluminijeve tarče, ogljikove ploščice in laserskega žarka

ever, a thin layer of recrystallized grains could be seen on the surface.

2.2 The target after irradiation

The laser-beam energy density on the aluminium target was not uniform over the cross-section of the focal spot [7]. The damage to the aluminium after irradiation with 3, 50 and 100 laser pulses with a repetition in frequency of 1 Hz were inspected in the area of the craters and on the parts in the direct vicinity of the maximum irradiation.

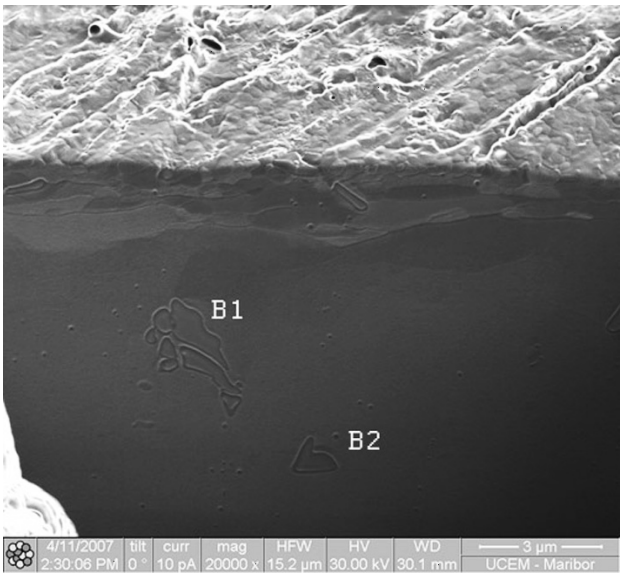

Figure 2: An overview of the Al surface and the direct area under the surface before irradiation with the laser beam. A thin and partly recrystallized surface layer is visible.
Slika 2: Pogled na površino Al in območja tik pod površino pred obsevanjem z laserskim žarkom. Viden je tanka površinska plast, ki je delno rekristalizirana

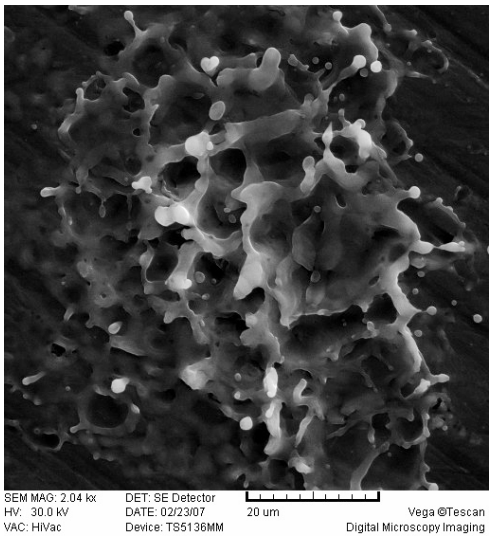

Figure 3: The target after three pulses (central part of the damage – maximum radiation) (SEM)
Slika 3: Tarča po treh impulzih (najbolj poškodovano območje, največje obsevanje žarčenje) (SEM)

The next three figures show the damage to the Al surface investigated by using the SEM. After three pulses (**Figure 3**) the target shows a melted surface as a consequence of the capillary waves. The "vertical" columns of relief, which appear due to Kelvin-Helmholtz instability, were observed. These occur at the interference between two layers, i.e., when the vapour velocity becomes much higher than the velocity of the liquid layer [8]. Therefore, the emission of droplets with radii between 0.1 µm and 0.5 µm is observed. **Figure 4** shows a deep crater formed on the target after 50 pulses. Additionally, a crater ring and a vortex formation of a self-organized closed loop of a vortex filament can be seen.

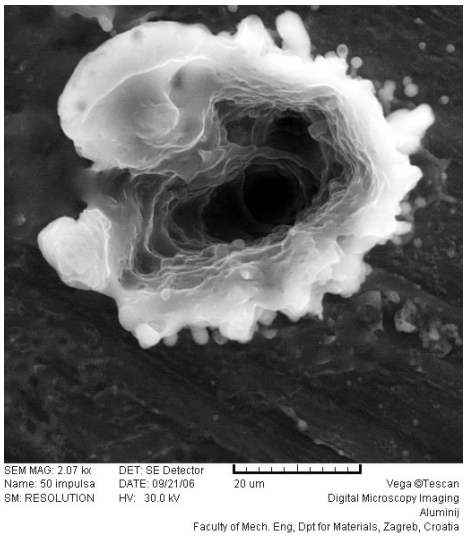

Figure 4: The target after 50 pulses (central part of damage) (SEM)
Slika 4: Tarča po petdesetih impulzih (najbolj poškodovano območje) (SEM)

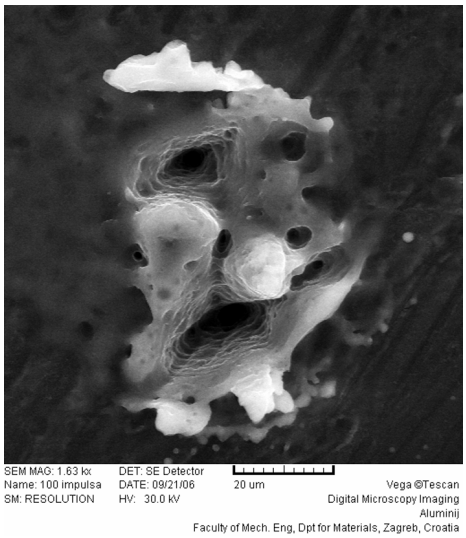

Figure 5: The target after 100 pulses (central part of damage) (SEM)
Slika 5: Tarča po stotih impulzih (najbolj poškodovano območje) (SEM)

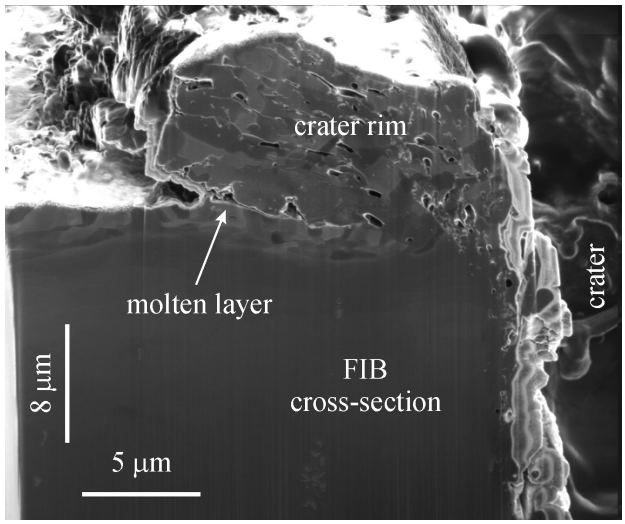

Figure 7: The Rayleigh-Taylor instability is visible on the side of the "deep" crater
Slika 7: Na stranici "globokega" kraterja je vidna Rayleigh-Taylorjeva nestabilnost

Furthermore, the crater formed after 100 pulses is shown in **Figure 5**. The crater rim is partially pushed away due to the pressure of the surrounding air and the laser-produced plasmas.

The FIB device was also used for the analysis of the laser ablation of the aluminium target situated in the air. After 50 pulses the damage at a depth of about 30 µm below the sample surface is shown in **Figures 6 and 7**. The vortex formation (**Figure 4**) and the crater configuration were caused by the Kelvin-Helmholtz and the Rayleigh-Taylor instabilities [8]. This process is analogous to the dense droplets that are instilled in the thin fluid. In other words, we take it that the laser pulses are like electromagnetic shots (or droplets). Each laser shot melts the aluminium and transforms it in a bulk, over vapour, mostly in a hot ionized gas (plasma), which is spread in all directions with a temperature gradient due to the developed plasma pressure. The distribution of the temperature establishes two types of hydrodynamic phenomena: one type in the "vertical" plane, i.e., the Kelvin-Helmholtz instability, and the other in the "horizontal" plane. The horizontal acceleration of the particles is the largest in the inner part and it decreases towards the periphery. The solidified gas builds a characteristic inner crater wall (**Figure 7**) and the vortices are the result. The gas also overheads the crater and builds the rim on the top. The gas and its

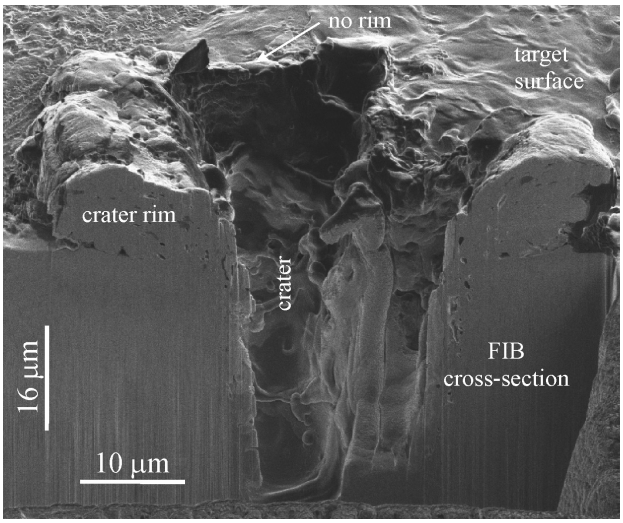

Figure 6: The Al crater after 50 pulses (FIB). Note that the length scale in the "horizontal" and "vertical" directions is not the same because the ion beam scanned the cross-section at an angle of 52°
Slika 6: Krater na aluminijevi tarči po petdesetih impulzih (FIB). Skali v vodoravni in navpični smeri nista enaki, ker je ionski curek skeniral prečni prerez pod kotom 52°

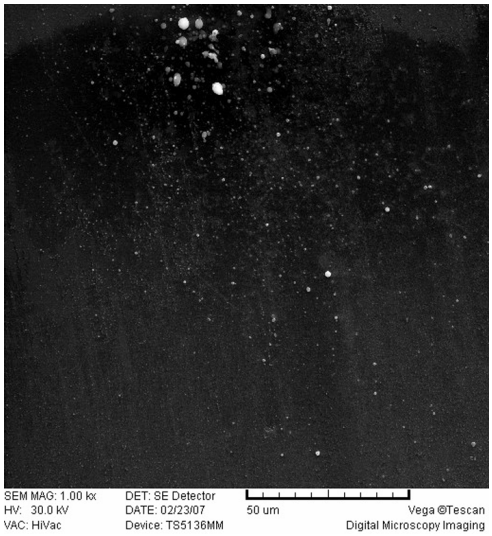

Figure 8: The traces of deposited plasma visible on the smooth glassy carbon plate
Slika 8: Na gladki steklasti ogljikovi ploščici so vidni sledovi nanosa plazme

Table 1: EDS Analysis. All elements analysed (Normalized)
Tabela 1: EDS-analiza

	Al	Si	Fe
Spectrum 1 / B1	64.90	4.42	30.69
Spectrum 2 / B2	71.93	4.05	24.03

All results in mass fraction (%)

Table 2: Aluminium Al
Tabela 2: Aluminij Al

Atomic mass	26.98
1. Ionization potential	5.999 eV
2. Ionization potential	18.83 eV
Heat of fusion	10.79 kJ/cal
Heat of vaporization	293.40 kJ/mol

conversions into droplets have been partly thrown out from the crater. The crater depth increases with the number of laser pulses while forming a narrow capillary. It can be concluded that the described process can be explained as a type of capillary discharge.

The particles of the bulk are ejected from the crater. They are deposited on the target surface and (**Figure 8**) on the smooth glassy carbon plate as frozen droplets. Their dimensions decrease with the distance of the crater.

2.3 Electron temperature of the aluminium plasmas

A feature of the developed plasmas, which is a consequence of the laser irradiation, is the electron temperature, T_e. For a target placed in vacuum this property was estimated using the theoretical formula known from literature [9,10]:

$$T_e/\mathrm{K} = 2.98 \cdot 10^4 \cdot A^{1/8} (Z+1)^{-5/8} \cdot Z^{1/4} (I \cdot \lambda)^{1/2} \cdot \tau^{1/4} \quad (1)$$

where A is the atomic weight of an ion, $Z = 1$ is the charge of the ion, known from a spectroscopic experiment [7]. Due to the fact that the second ionization potential of Al is ≈ 19 eV (**Table 2** [11]), multiple ionization has been neglected and only simple charge ions have been considered. (We found ions with the charge $Z = 2$ only in the titanium plasma produced by this nitrogen laser. The energy deposition was more effective than in other cases since the wavelength of the laser is in the vicinity of the Ti resonance lines [12]). The number density of the electrons (N_e) is equal to the number density of the ions (N_i), i.e., $N_i \approx N_e$.

In Equation (1), $\lambda = 337 \cdot 10^{-7}$ cm is the radiation wavelength, $\tau = 6 \cdot 10^{-9}$ s is the laser pulse duration and I is the absorbed laser-radiation intensity ($1.3 \cdot 10^8$ W/cm^2), reduced by about 5 %. In other words, the laser-absorbed pulse energy is released by the heat of fusion, the heat of vaporization, the ionized energy and the plasma energy. The ejected volume was evaluated from the Al target after 50 laser irradiations (pulses), as shown in **Figure 6**. Using **Table 2** the thrown mass/pulse is ≈ $1.32 \cdot 10^{-11}$. Therefore, from **Table 2**, the calculated heat of fusion is ≈ $1.4 \cdot 10^{-4}$ J/pulse, the heat of vaporization is ≈$3.9 \cdot 10^{-6}$ J/pulse, and the ionized energy is ≈$7.6 \cdot 10^{-6}$ J/pulse. The above-mentioned energies are about 5 % of the total pulsed-laser energy. Therefore, the laser-generated plasma converts significant amounts of the absorbed laser energy at the Al target into the energy of plasma particles.

From Equation (1) the electron temperature for the aluminium plasma with single ionized atoms is (1.4 ± 0.1) eV. This is somewhat lower than the temperature measured by means of the spectral lines [7] when the Al target is located in air at normal pressure. Furthermore, the aluminium ablation will be compared with the model prediction made by S. Amoroso [13]. The ejected mass is composed of electrons, excited neutrals, ground-state neutrals and ions. The vapour breakdown occurs within ≈1 ns and the electron temperature strongly increases from the low value up to a calculated 1.4 eV. The temperatures of the electrons and the massive particles become nearly the same, reaching an equilibrium condition in a time interval close to the laser-pulse duration.

3 CONCLUSION

The laser irradiation of the aluminium surface in air at normal pressure caused the modification of the target, and the explosion of plasma mixed with expanding target droplets. After a few pulses, the ablated surface shows the topology produced by the Kelvin-Helmholtz instability. Subsequent laser pulses resulted in the formation of a crater in the area irradiated by highest energy density. The crater is surrounded by a rim that was formed presumably due to the Kelvin-Helmholtz and the Rayleigh-Taylor instabilities. The rim was partly pushed away after a number of pulses, (approximately 100). The surface of the glassy carbon plate was covered by a thin aluminium film containing numerous droplets. The applied set-up shows that there is a possibility of depositing a thin film.

A small discrepancy between the theoretical electron temperature and the measured value is expected and it can be explained by the presence of air at normal pressure where the target was situated. In our earlier investigations with other targets (e.g., Ti, Cu [12,14]) we noticed that the obtained temperatures are 10 % higher than in vacuum, i.e., (1.5 ± 0.1) eV for aluminium.

Acknowledgement

The authors gratefully acknowledge the assistance that was kindly provided by Prof. H.-J. Kunze, Nikolina Volf and Iva Orhanović.

4 REFERENCES

[1] M. Von Allmen, Laser Beam Interaction with Materials, Springer, Heidelberg 1987

[2] V. Khomchenko at al. Appl. Surface Science, 247 (**2005**) 434

[3] S. S. Harilal. C. V. Bindhu. M. S. Tillack, F. Najmabadi, A. C. Garis, J. Appl. Phys. 93 (**2003**), 2380

[4] R. E. Russo, Appl. Spectrosc. 49 (**1995**), 14A

[5] I. I. Beilis, Laser and particles beams 25 (**2007**), 53

[6] R. K. Tharea, A. K. Sharma, Plasma Science, IEEE Conf. Record-Abstracts (**2004**), 263

[7] Ž. Andreić, V. Henč-Bartolić, H.-J. Kunze, Physica Scripta 48 (**1993**), 331

[8] S. Lugomer, Laser matter interaction, Profil, Zagreb 2001

[9] O.A. Novodvorsky. C. Wenzel, J.W. Bartha, O.D. Khramova, E.O. Filippova, Optics and Lasers in Engineering 36 (**2001**) 3, 303

[10] O. A. Novodvorsky, O.D. Khramova, C. Wenzel, J.W. Bartha. E.O. Filippova, J. of Appl. Phys. 94 (**2003**) 5, 3612

[11] http://pol.spurious.biz/projects/chemglobe

[12] V. Henč-Bartolić, Ž. Andreić, H.-J. Kunze, Physica Scripta 59 (**1994**), 368

[13] S. Amoruso, Appl. Phys. A 69 (**1999**) 323

[14] V. Henč-Bartolić, Ž. Andreić, M. Stubičar, H.-J. Kunze, Fizika A 7 (**1998**) 4, 205

UDK 669.862'782'783:620.18
Original scientific article/Izvirni znanstveni članek

ISSN 1580-2949
MTAEC9, 42(3)117(2008)

CHANGES IN THE MICROSTRUCTURE OF Fe-DOPED $Gd_5Si_2Ge_2$

SPREMEMBE V MIKROSTRUKTURI ZLITINE $Gd_5Si_2Ge_2$, DOPIRANE Z Fe

Irena Škulj[1], Paul McGuiness[2], Benjamin Podmiljšak[2]

[1]Institute of Metals and Technology, Ljubljana, Lepi pot 11, 1000 Ljubljana, Slovenia
[2]Jožef Stefan Institute, Jamova 39, 1000 Ljubljana, Slovenia
irena.skulj@imt.si

Prejem rokopisa – received: 2008-01-03; sprejem za objavo – accepted for publication: 2008-03-25

$Gd_5Si_2Ge_2$-based alloys can exhibit a giant magnetocaloric effect (MCE); this gives them the potential for use in cooling and refrigeration technologies. Cast alloys of this type have been reported to exhibit a three-phase microstructure: the main phase has a composition close to $Gd_5(Si_{1.95}Ge_{2.05})$; the secondary phases are $Gd_1(Si,Ge)_1$ and $Gd_5(Si,Ge)_3$, with the latter reported to have linear features in the microstructure, characteristic of a Widmanstätten pattern. In this investigation we have looked at the effect on the microstructure of $Gd_5Si_2Ge_2$ resulting from a substitution of Si by Fe, according to the formula $Gd_5Si_{2-x}Fe_xGe_2$, where x was varied between 0 and 1. Alloys with six different compositions were prepared using the arc-melting technique. All the samples and their microstructures were observed examined in optical microscope (OM) and a field-emission-gun scanning electron microscope (FEG SEM). The microstructures were quantitatively assessed with energy-dispersive X-ray spectroscopy (EDS) and the samples were characterised using X-ray diffraction (XRD).

Keywords: magnetocaloric effect, microstructure, $Gd_5Si_2Ge_2$-type alloys

Zlitine $Gd_5Si_2Ge_2$ imajo dobre magneto-kalorične lastnosti (MCE) in so zaradi tega potencialno uporabne v hladilni in zmrzovalni tehnologiji. Lite mikrostrukture teh zlitin imajo večfazno strukturo, in sicer jo sestavljajo glavna faza s sestavo blizu $Gd_5(Si_{1.95}Ge_{2.05})$ in dve sekundarni fazi $Gd_1(Si,Ge)_1$ in $Gd_5(Si,Ge)_3$. V mikrostrukturi je opaziti fazo podolgovate oblike, ki jo lahko označimo kot Widmanstättenov vzorec. V delu teh raziskav smo se posvetili raziskavam sprememb mikrostrukture zlitine $Gd_5Si_2Ge_2$, ko v sestavi Si nadomeščamo z Fe. Sestave vzorcev ustrezajo $Gd_5Si_{2-x}Fe_xGe_2$, kjer smo vzeli vrednosti x med 0 in 1. Zlitine vseh šestih različnih sestav smo pripravili z obločnim taljenjem. Njihove mikrostrukture smo pregledali v optičnem mikroskopu (OM) in vrstičnim elektronskem mikroskopu na poljsko emisijo (FEG SEM). Mikrostrukture smo kvantitativno analizirali z energijsko disperzivnim spektrometrom (EDS) in faze identificirali z rentgensko spektrometrijo (XRD).

Ključne besede: magneto-kalorimetrija, mikrostruktura, zlitine $Gd_5Si_2Ge_2$

1 INTRODUCTION

The discovery of $Gd(Si_xGe_{1-x})_4$ alloys goes back to the late 1960s [1,2]. Gd_5Si_4 orders ferromagnatically at Tc = 335 K, and as much as 50 % of the Si can be substituted while maintaining the magnetic properties and the orthorhombic structure. Percharsky and Gschneidner [3] were, however, the first to report a large, near-room-temperature magnetocaloric effect (MCE) in these alloys.

$Gd_5Si_2Ge_2$-type alloys with a monoclinic structure at room temperature all exhibit the giant magnetocaloric effect, from 46 J/(kg K) at 195 K to 16 J/(kg K) at 310 K [4]. The temperature at which the large magnetocaloric effect is observed can be easily adjusted between ≈ 190 K and 300 K by varying the chemical composition, i.e., by varying the Si/Ge ratio between 0.6 and 1.1.

Reversible first-order transitions from ferromagnetic to paramagnetic (FM↔PM) for $Gd_5(Si_xGe_{1-x})_4$ where $0.37 \leq x \leq 0.52$ can be induced by either temperature or magnetic field [5]. The co-existence of both FM and PM phases indicates the formation of a heterogeneous system with magnetically ordered and magnetically disordered phases. The application of a magnetic field to the PM regions restores the FM phase by shifting the T_C.

These alloys form $Gd_5Si_2Ge_2$-type columnar cellular grains as the matrix phase and some additional phases located along the grain boundaries [6]. The additional phases are known as the GdGe- and $GdSi_{2-x}$-type phases. The room-temperature matrix monoclinic phase transforms into the orthorhombic Gd_5Si_4-type phase during cooling, without any apparent microstructural changes.

At low temperatures $Gd_5(Ge_{1-x}Si_x)_4$ adopts an orthorhombic Gd_5Si_4-type structure, and the ground state is ferromagnetic [7]. At room temperature three different structures were observed, depending on the composition. For $x > 0.55$ the Gd_5Si_4 structure is stable, for $x < 0.3$ the Sm_5Ge_4-type structure was observed, and for $0.3 < x < 0.55$ the $Gd_5Si_2Ge_2$-type structure with an intermediate volume is formed. These three structures types are closely related. All three unit cells contain four formula units and essentially only differ in the mutual arrangement of identical building blocks, which are either connected by two, one or no covalent-like Si-Ge bonds, resulting in successively increasing unit-cell volumes [7,8].

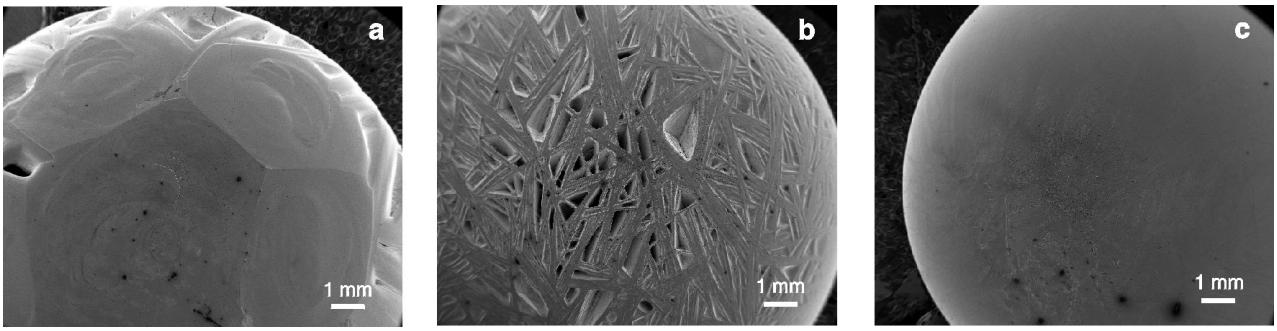

Figure 1: SEI taken of arc-melted buttons with G_0 (a), G_2 (b) and G_4 (c) compositions
Slika 1: SEM-posnetki obločnotaljenih vzorcev s sestavami G_0 (a), G_2 (b) in G_4 (c)

2 EXPERIMENTAL DETAILS

The compositions studied in this research were $Gd_5Si_{2-x}Fe_xGe_2$ with x = 0, 0.125, 0.25, 0.5, 0.75 and 1. All the compositions of the samples are collected in **Table 1**, together with the respective sample codes, G_0, G_{05}, G_1, G_2, G_3, and G_4. All the samples were prepared from high-purity starting elements with the mass fractions of gadolinium (99.99 %), silicon (99.995 %), germanium (99.999 %) and iron (99.99 %). The samples were prepared by arc-melting a mixture of pure elements on a water-cooled copper hearth in an argon atmosphere with a pressure of 0.5 bar. Each sample was re-melted three times and after each re-melting the samples was turned over to ensure their homogeneity. All the samples were prepared as 5 g buttons.

Table 1: The compositions of all alloys used in this work in the mole fractions (%)
Tabela 1: Sestave vzorcev, uporabljenih v raziskovalnem delu v molskih deležih (%)

	Gd	Si	Fe	Ge
G_0	55.6	22.2	/	22.2
G_{05}	55.6	20.8	1.4	22.2
G_1	55.6	19.4	2.8	22.2
G_2	55.6	16.6	5.6	22.2
G_3	55.6	13.9	8.3	22.2
G_4	55.6	11.1	11.1	22.2

All the samples were cut and cross-sectioned, and then polished for the optical and electron microscopy. All the microstructures were inspected with an optical microscope and quantitatively assessed with a FEG SEM, with all the phases analysed with EDS. All the XRD patterns for all the samples were collected using Cu-Kα radiation.

3 RESULTS

3.1 Microstructure

The electron microscopy SE images in **Figure 1** show the macrostructures of three of the arc-melted buttons. The differences in the upper surfaces of the button sample are strikingly different. The G_0 sample exhibits regular pentagons and hexagons reminiscent of a buckyball. The G_2 sample's surface shows a sinew effect, rather like columnar grains running at angles on the upper surface of the sample. The G_4 sample has a smooth upper surface, much more characteristic of an intermetallic arc-melted button.

Optical micrographs taken of the set of $Gd_5Si_{2-x}Fe_xGe_2$ samples with x = 0, 0.125, 0.25, 0.5, 0.75 and 1 are shown in **Figure 2**. It is clear from the six images that all the samples consist of multi-phase structures. The microstructure of the G_0 sample, where x = 0, consists of the $Gd_5(Si,Ge)_4$ matrix phase A and a grain-boundary phase. A new matrix phase, the B phase, appears with the smallest addition of iron, i.e., the G_{05} sample. The composition of the matrix phase B suggest that it is a $Gd_5(Si,Ge)_3$-type phase. With increasing

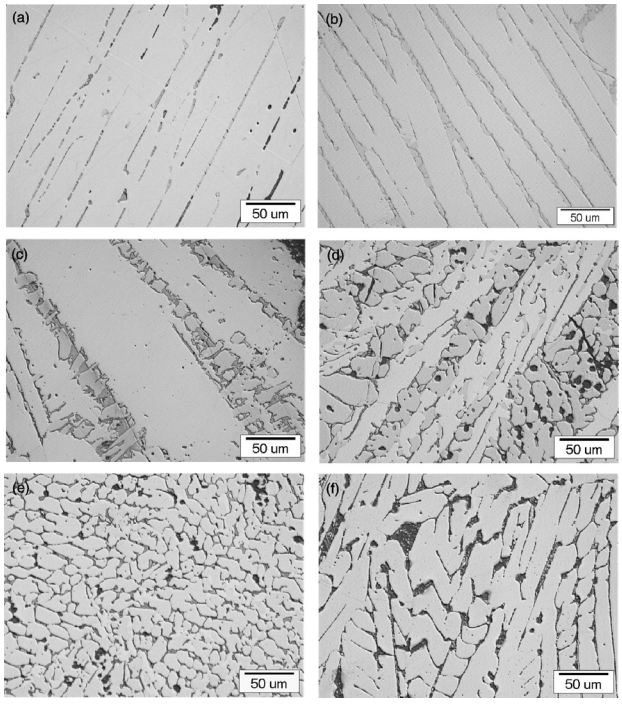

Figure 2: Optical images of the etched microstructures of arc-melted G_0 (a), G_{05} (b), G_1 (c), G_2 (d), G_3 (e) and G_4 (f) samples
Slika 2: Optični posnetki jedkanih mikrostruktur obločnotaljenih vzorcev G_0 (a), G_{05} (b), G_1 (c), G_2 (d), G_3 (e) in G_4 (f)

amounts of added iron the amount of matrix phase A is seen to decrease until it disappears completely in sample G_4, the point where half of silicon is replaced by iron. It is also worth noting that approximately half of the matrix phase A is replaced by matrix phase B in the G_2 sample with $x = 0.5$.

3.2 Phase compositional analyses

The compositions of the matrix phases A and B with respect to the amount of added iron can be seen in **Table 2**. The compositions strongly suggest that matrix phase A is a Gd_5Si_4-type phase, while matrix phase B is better described by the composition Gd_5Si_3. The amount of the dissolved Fe in both of the matrix phase varies. In both cases the amount of Fe in the matrix phases increases with the increasing amount of added iron; however, there is some variability in the analyses. This is particularly so for the amount of Fe dissolved in matrix phase B. It should be noted, however, that the amounts of iron in the matrix phases are very low; in all cases the mole fraction is <1.5 %.

The compositions of the grain-boundary phases analysed for all six samples are collected in **Table 3**. Three different grain-boundary phases were identified. The grain-boundary phase found in sample G_0 is not significantly different from that of the matrix phase, and this phase is only present in this sample, the one with no iron in the initial composition. The grain-boundary phase GB2 appears in all the samples with any amount of iron present in the initial composition. The composition of this GB2 phase does not vary with increasing amounts of added Fe, and the ratio for Gd:Si:Fe is approximately 1:1:1. The grain-boundary phase GB3 starts forming in the structure of the samples as a grain-boundary phase when x becomes larger than 0.5, i.e., in samples G_3 and G_4. The composition of the GB3 phase was different for the two samples, but in this case the values of the mole fractions are very high, i.e., >50 %.

3.3 XRD

The XRD patterns of the as-arc-melted button samples can be seen in **Figure 3**. The peaks in the pattern that belongs to the G_0 sample confirm that the main phase seen in the microstructure (**Figure 2a**) is the $Gd_5Si_2Ge_2$ monoclinic phase. The vast majority of the

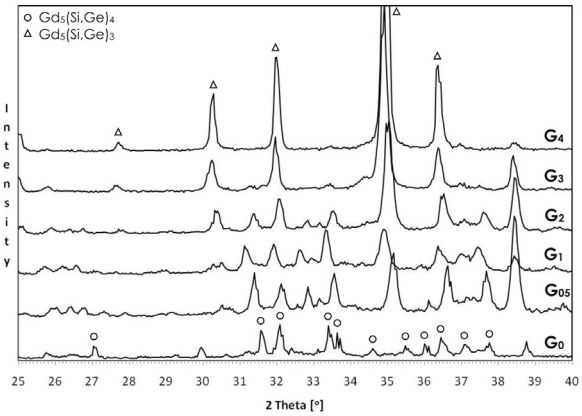

Figure 3: XRD patterns of arc-melted samples
Slika 3: Rentgenski spektri obločnotaljenih vzorcev

Table 2: Elemental compositions in mole fractions (%) of the two main phases present in the samples evaluated using EDS. Analysing errors to be considered are Gd ±0.2, Si ±0.1, Fe ±0.2 and Ge ±0.3.
Tabela 2: Elementarne sestave v molskih deležih (%) obeh glavnih faz v mikrostrukturah, pridobljenih z EDS. Napake pri analizah so: Gd ±0,2, Si ±0,1, Fe ±0,2 in Ge ±0,3

	Phase A				Phase B			
	Gd	Si	Fe	Ge	Gd	Si	Fe	Ge
G_0	55.8	23.7	/	20.5	–			
G_{05}	55.2	20.7	0.5	23.6	61.5	16.1	0.6	21.8
G_1	56.2	20.0	0.5	23.3	62.8	16.2	1.0	20.6
G_2	56.2	17.6	0.8	25.4	63.2	13.8	0.6	22.4
G_3	56.3	15.2	0.7	27.8	61.8	11.1	0.7	26.4
G_4	–				61.8	11.7	1.3	25.2

Table 3: Elemental compositions in mole fractions (%) of the grain-boundary phases present in the samples evaluated using EDS. Analysing errors to be considered are Gd ±0.2, Si ±0.1, Fe ±0.2 and Ge ±0.3.
Tabela 3: Elementarne sestave v molskih deležih (%) faz na mejah med kristalnimi zrni glavnih faz, pridobljenih z EDS. Napake pri analizah so: Gd ±0,2, Si ±0,1, Fe ±0,2 in Ge ±0,3

	GB phase 1				GB phase 2				GB phase 3			
	Gd	Si	Fe	Ge	Gd	Si	Fe	Ge	Gd	Si	Fe	Ge
G_0	51.5	31.7	/	17.0	–				–			
G_{05}	–				34.8	27.4	33.3	4.5	–			
G_1	–				35.5	28.0	30.8	5.6	–			
G_2	–				35.5	26.9	31.7	5.9	–			
G_3	–				35.3	26.3	31.4	7.0	33.1	5.5	59.9	1.5
G_4	–				33.2	28.3	34.5	4.0	31.3	13.2	53.1	2.5

peaks agree with the calculated pattern for the $Gd_5Si_2Ge_2$ compound. The positions of the calculated peaks are identified by the circles in **Figure 3**. New peaks can be observed in the other patterns as a result of the formation of new phases in all the samples with added iron, i.e., where $x \neq 0$. Some shifts in the peaks, while maintaining the same structure, can also be seen, and these shifts result from the iron entering both A and B matrix phases and forming solid solutions. The pattern of the G_4 sample indicates that the matrix phase B is the only matrix phase still present in the sample.

4 DISCUSSION

The unusual macrostructural features observed for the samples with no iron and very small amounts of iron are very striking; however, during our microstructural investigations on cross-sections near the surface, these features were found to penetrate only short distances into the sample, and in no way were they representative of the bulk. The formations – the buckyballs and the sinews – are clearly related to the cooling rate, which is very fast in such a system, but very small amounts of iron are clearly the decisive factor. The very high aspect ratios of the sinews are indicative of strongly anisotropic grain grown on the sample's surface, which must be a consequence of the dissolved iron, whereas the buckyballs point to a surface-energy effect, with the flat surfaces representing the growth of particular atomic planes. The smooth surface of the G_4 sample implies that minimising surface area during the molten phase is still the predominant factor in determining the final shape of the solid button.

The optical micrographs in **Figure 3** show the gradual changes with compositional variations. The second matrix phase, B, begins to form between the grains of the original matrix phase, A, and then gradually comes to dominate the microstructure as the amount of iron in the sample increases. The EDS measurements clearly reveal the presence of iron in both matrixes A and B. However, the amount in the mass fractions of iron does not vary much, being between 0.5 % and 1.3 % for both phases in all the samples. Much more dramatic changes are seen in the amounts of Si and Ge in the matrix phases. In both cases the addition of iron at the expense of Si causes Ge to substitute for the Si: in the G_{05} sample, for example, the relative amounts of Si and Ge in the two phases, A and B, were 20.7 : 23.6 and 16.1 : 21.8 respectively. By the time we reach sample G_3, the ratios have shifted to samples that are much richer in Ge, i.e. 15.2 : 27.8 and 11.1 : 26.4.

The XRD diffraction results are very clear in the case of the two matrix phases. The gradual disappearance of the $Gd_5Si_2Ge_2$ phase as the iron is added, and the parallel growth of the $Gd_5(Si,Ge)_3$ phase are easily seen. Unfortunately, however, the XRD data does not give us any help when trying to obtain structural information on the grain-boundary phases.

5 CONCLUSIONS

It can be concluded that the $Gd_5Si_{(2-x)}Fe_xGe_2$ alloys where x varies between 0 and 1 show significant differences in both macrostructures and microstructures. The A matrix phase with the $Gd_5(Si,Ge)_4$ composition when $x = 0$ becomes the B matrix phase with the $Gd_5(Si,Ge)_3$ composition when $x = 1$. All the samples with x between 0 and 1 show the presence of both matrix phases in the alloy. The substituted iron was found in all the matrix and grain-boundary phase, although the amounts in the matrix phases where very low. The iron contributes mainly to the grain-boundary phases that are formed and to a change in the relative amounts of Si and Ge in the matrix phases.

6 REFERENCES

[1] F. Holtzberg, R. J. Gambino, T. R. McGuire, J. Phys. Chem. Solids, 28 (**1967**), 2238
[2] G. S. Smith, A. G. Tharp, Q. Johnson, Acta Crystallogr., 22 (**1967**), 940
[3] V. K. Pecharsky, K. A. Gschneider Jr.: Phys. Rev. Lett., 78 (**1997**), 4494
[4] A. O. Pecharsky, K. A. Gschneider Jr., V. K. Pecharsky, JMMM, 267 (**2003**), 60
[5] E. M. Levin, K. A. Gschneider Jr., V. K. Pecharsky, JMMM, 231 (**2001**), 135
[6] H. Fu, Y. Chen, M. Tu, T. Zhang, Acta Materialia, 53 (**2005**), 2377
[7] A. O. Percharsky, K. A. Gschneider, V. K. Percharsky, C. E. Schindler, J. Alloys Compounds, 338 (**2002**), 126
[8] Y. Mozharivskyj, A. O. Percharsky, V. K. Percharsky, G. J. Miller, J. Am. Chem. Soc., 127 (**2005**), 317

UDK 669.14:620.18:620.17:621.73
Original scientific article/Izvirni znanstveni članek

ISSN 1580-2949
MTAEC9, 42(3)121(2008)

DEVELOPMENT OF MICROSTRUCTURE DURING THE HOT PLASTIC DEFORMATION OF HIGH CLEAN STEELS FOR POWER PLANTS

RAZVOJ MIKROSTRUKTURE MED VROČO PLASTIČNO DEFORMACIJO VISOKO ČISTEGA JEKLA ZA ENERGETSKE NAPRAVE

Kuskulic, Tomas[1], Kvackaj, Tibor[1], Fujda, M.[1], Pokorny, I.[1], Bacsó J.[1], Molnarova, M.[1] Kocisko, R.[1], Weiss, Michael[2], Bevilaqua, Tomas[2]

[1] Technical university of Košice, Letna 9, 04200 Košice, Slovakia
[2] ZP-Podbrezova a.s., Kockaren 35, 97681 Podbrezova, Slovakia

Prejem rokopisa – received: 2007-09-28; sprejem za objavo – accepted for publication: 2008-01-11

The effect of the deformation and the deformation temperature on the primary austenite grain size, the recrystallisation and the mechanical properties of high clean steel STN 41 6537 (STN standard) were investigated. This steel grade is used for the forged rotors of steam turbines in power-generation facilities.

Key words: steel, power generation, forging, recristallisation, mechanical properties

Raziskan je bil vpliv deformacije in deformacijske temperature na velikost avstenitnih zrn, rekristalizacijo in mehanske lastnosti zelo čistega jekla STN 416537 (STN standard). To jeklo se uporablja za kovane rotorje parnih turbin pri proizvodnji električne energije.

Ključne besede: jeklo, proizvodnja energije, kovanje, rekristalizacija, mehanske lastnosti

1 INTRODUCTION

The world is characterised by a constantly increasing population and a demand for improved living conditions. The industrialisation of a country depends strongly on the availability of electrical energy, which plays a key role in the rate of development[1].

Modern high-pressure steam turbines operate under high working loads and at high temperatures. For this reason, much concern has been paid to the fatigue and creep behaviours of turbine materials. The rotor of a steam turbine also operates at high temperatures, and during complex stressing some cracks are likely to initiate. In addition to fatigue, creep damage plays an important role in rotor damage. Generally speaking, low-cycle fatigue uses up seventy percent of the life of the rotor, and creep accounts for the remaining thirty percent[2]. However, fatigue and creep always occur together, and the coupling of fatigue and creep must be considered in the lifetime prediction of a steam-turbine rotor[3].

Much effort has been spent on developing a new, high-strength ferritic resistant steel, which would also be used for large components of fossil-fuel-fired power plants[4]. Because of the degradation during long-term service at elevated temperatures that causes changes in the microstructure[5], an improvement in microstructural stability is a prerequisite for achieving excellent long-term creep strength. New steels have been widely used in modern fossil-fuel-fired power plants and in many investigations the correlations between the microstructure and the mechanical properties have been reported[6].

The hot-working behaviour, in conjunction with the changes in the microstructure and the degradation during long-term creep deformation, is investigated and discussed in this article.

2 MATERIAL AND EXPERIMENTS

For the experiments a steel based on CrNiMoV was used; this is equivalent to STN 41 6537, with the chemical composition described in **Table 1**.

Table 1: Chemical composition
Tabela 1: Kemična sestava

C	Mn	Si	P	S	Cr	Ni	Cu	Mo	V	Al	As	Sn	Sb	Ca	H	N	O
w/%											μg/g						
0.29	0.04	<0.01	0.003	0.003	1.57	2.84	0.010	0.39	0.11	0.004	11	8	<5	20	0.5	44	25

The experiments were designed to determine the influence of temperature and deformation on the austenite grain size. For the tests on the influence of the finish forging temperature and the final amount of deformation on the evolution of austenite grain size, the hot-working schedule in **Figure 1** was applied. The experimental samples of size (26 × 30 × 55) mm were heated under controlled conditions in air and cooled down to the first deformation temperature $T_{\varepsilon 1}$ = 1100 °C in $t_{1,\text{hold}}$ = 22 s and then deformed for ε_1 = 50 %. The first plastic deformation was followed by holding the samples at the second deformation temperature $T_{\varepsilon 2}$ in a chain conveyer furnace for $t_{2,\text{hold}}$ = 80/100/120/150 s. Afterwards, the forgings were cooled from $T_{\varepsilon 1}$ to $T_{\varepsilon 2}$ = (800/850/900/950) °C and then submitted to a second plastic deformation ε_2 = (10/20/30/40/50/60) % and finally quenched in a KOH water solution. Next the samples were ground and polished and annealed at 550 °C for 48 h. After annealing the continuous layer of scale was removed with fine grinding and the grain boundaries revealed with stringers of oxide particles. Finally, the specimens were etched in a water solution of picric acid with the addition of CuCl and the microstructure was investigated with optical microscopy. The size of the statically recrystallised austenite grains was assessed with a linear method as an average of 20 measurements. In cases of the absence of static recrystallization of the austenite the average corrected austenite grain diameter was calculated from equations based on an assessment of the average effective nucleation area.

$$d_{\gamma,\text{kor}} = \frac{2000}{Sv(\text{gb}+\text{db})} \tag{1}$$

$$Sv(\text{gb}+\text{db}) = 1000\cdot\left[0{,}429\cdot(d_{\gamma,0}) + 1{,}571(d_{\gamma,\perp})\right] = \\ = \frac{1000}{d_{\gamma,0}}\cdot\left[0{,}429\cdot(1-\varepsilon_0) + \frac{1{,}571}{(1-\varepsilon_2)}\right] \tag{2}$$

where:

$d_{\gamma,\text{kor}}$/μm is the corrected average diameter of an austenite grain,

$d_{\gamma 0}$/μm is the recrystallised diameter of an austenite grain before the thermal area of the inhibited austenite recrystallisation.

Sv(gb+db) /(1/mm) is the average effective nucleation area of the grain boundaries and deformation bands,

Sv(gb) is the effective nucleation area of the grain boundaries,

Sv(db) is the area of the deformation bands inside the austenite grains,

ε_2/% is the relative deformation.

In the case of static recrystallization of the austenite, the austenite grain diameter was deduced by applying the equation:

$$d_y = \frac{(1{,}68\cdot d_{\text{kr}})}{(n\cdot zv)} \tag{3}$$

where:

d_γ/μm is the austenite grain diameter,

d_{kr}/mm is the diameter of the circumference,

n is the number of intersected grain boundaries,

zv is the magnification.

The determined and deduced values for the grain size were then processed using non-linear numerical statistical methods and correlation equations for a description of the investigated dependences were generated.

3 RESULTS AND DISCUSSION

The influence of the final deformation and temperature on the austenite grain size is shown in **Figure 2 and 3**.

The obtained results show that with an increase in the amount of deformation ε_2 above 10 % and deformation temperature $T_{\varepsilon 2}$ above 850 °C the austenite grain diameter decreased from the original size $d_{\gamma 1}$ = 43 μm after the first plastic deformation to $d_{\gamma 2}$ = 7.7 μm for $T_{\varepsilon 2}/\varepsilon_2$ =

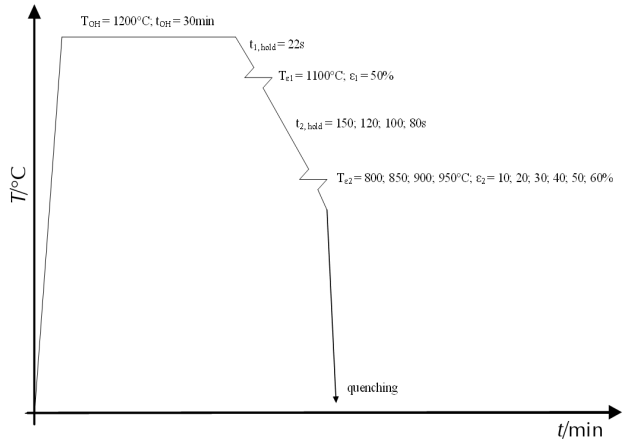

Figure 1: Temperature and deformation regime
Slika 1: Režim temperature in deformacije

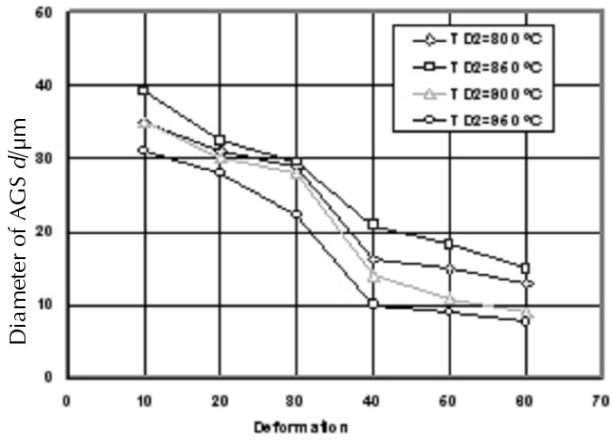

Figure 2: Dependence of AGS on deformation
Slika 2: Odvisnost AGS (velikost avstenitnih zrn) od deformacije

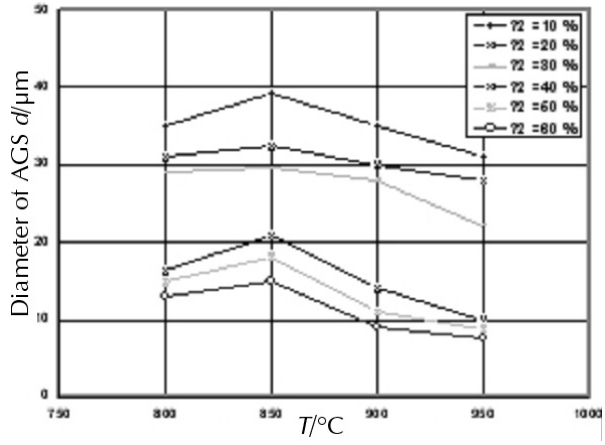

Figure 3: Dependence of AGS on deformation temperature
Slika 3: Odvisnost AGS od temperature deformacije

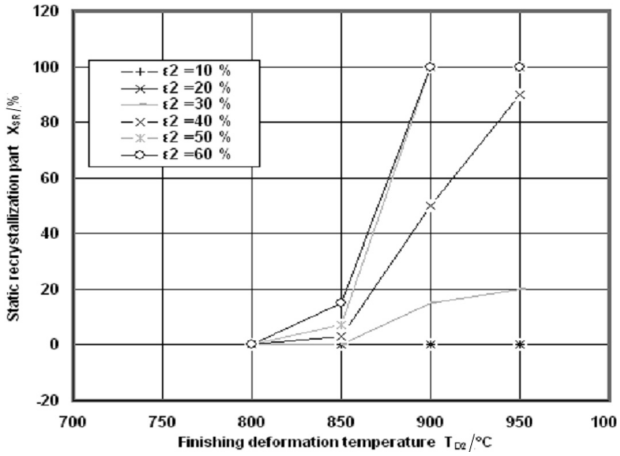

Figure 5: Dependence of X_{SR} on temperature
Slika 5: Odvisnost *X*sr od temperature

950 °C/60 %, or to the size of $d_{\gamma 2}$ = 15.0 µm for $T_{\varepsilon 2}/\varepsilon_2$ = 850 °C/60 %.

– for ε_2/% ∈ <10;30> and the investigated temperature $T_{\varepsilon 2}$/°C ∈ <800;950> the diameter of the austenite grain achieved coarse values of $d_{\gamma 2}$/µm ∈ <2.2;39.3>. For ε_2/% ∈ <40;60> and $T_{\varepsilon 2}$/°C ∈ <800;950> the diameter of the austenite grains achieved bottom values of $d_{\gamma 2}$ ∈ <7.7; 20.9> µm.

For an explanation of the occurrence of two areas of austenite grain size it was necessary to determine the share of static recrystallised austenite after the second deformation. The influence of the deformation ε_2 and of the deformation temperature $T_{\varepsilon 2}$ on the share of the static recrystallisation of austenite is shown in **Figures 4 and 5**.

– For the deformation ε_2/% ∈ <10;30> and the temperature $T_{\varepsilon 2}$/°C ∈ <800;950> the share of statically recrystallised austenite was of X_{SR}/% ∈ <0;20>.
– For the deformation ε_2/% ∈ <40;60> and the temperatures $T_{\varepsilon 2}$ = 800 °C and 950 °C the share of statically recrystallised austenite was in the range of X_{SR}/% ∈ <50;100> and it was classified as partly or completely recrystallised.

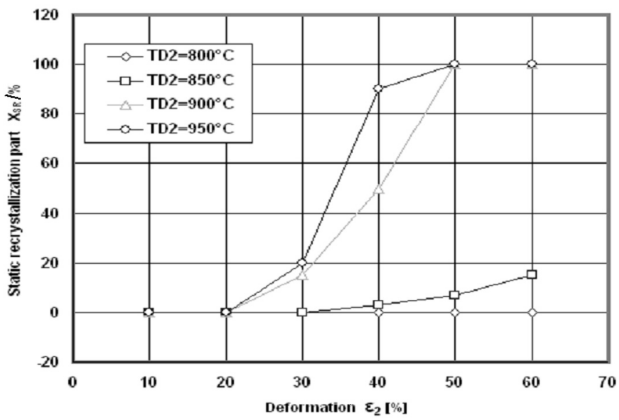

Figure 4: Dependence of X_{SR} on deformation
Slika 4: Odvisnost *X*sr (deleža rekristalizacije) od deformacije

– For the deformation ε_2/% ∈ <50;60> and the deformation temperatures $T_{\varepsilon 2}$ = 900 °C and 950 °C the share of statically recrystallised austenite was of X_{SR} = 100 % and it was classified as completely recrystallised.
– For the deformation of ε_2 = 40 % and the temperature of $T_{\varepsilon 2}$ = 950 °C the share of statically recrystallised austenite was of X_{SR} = 90 %, and it is also classified as completely recrystallised.

It can be concluded that the best conditions for attaining a completely statically recrystallised austenite are a deformation of ε_2 = 50 and 60 % at $T_{\varepsilon 2}$ = 900 °C and 950 °C. In this case the size of the austenite grain is in the range $d_{\gamma 2}$ = 7.7–11.0 µm.

Also, the static recrystallisation of austenite of (X_{SR} ≥ 90 %) is achieved for a deformation of ε_2 = 40 % and a temperature of $T_{\varepsilon 2}$ = 950 °C; however, the attained size of the austenite grain is $d_{\gamma 2}$ = 10 µm.

The experimental numerical data were processed using linear and non-linear statistical methods, and the dependence of the final temperature, the amount of deformation and the austenite grain diameter were determined. Two equations were obtained for the dependence $d_{\gamma 2} = f(\varepsilon_2; T_{D2})$.

1) Equation

$$d_{\gamma 2} = A0 \times T_{D2}^{A1} \times \varepsilon_2^{A2} \quad (4)$$

where:
T_{D2}/°C is the second deformation temperature,
ε_2/% is the relative deformation,
$A0 = 2.54585 \times 10^7$
$A1 = -2.2021262$
$A2 = -0.697277$

A graphical comparison of the calculated and measured values is shown in **Figure 6**. For the deformation of ε_2 = 30 % a strong deviation is found.

2) Equation

$$d_{\gamma 2} = B0 \times \ln\left[1/(1-\varepsilon)\right]^{B1} \times Z^{B2} \quad (5)$$

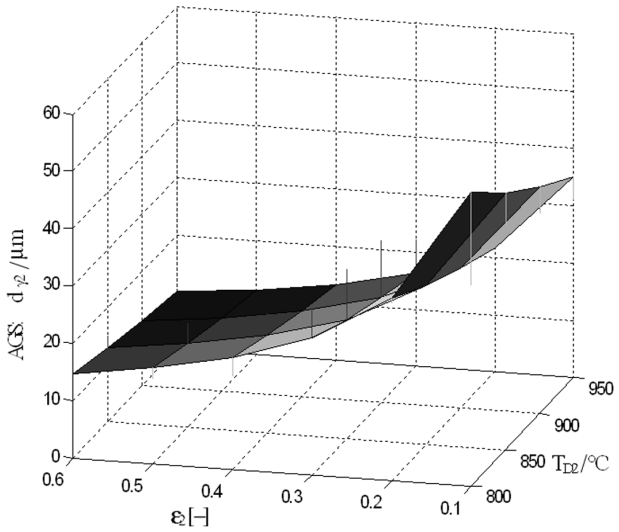

Figure 6: Comparasion of measurement and calculated values for equation
Slika 6: Primerjava meritev in izračunov z enačbo (4)

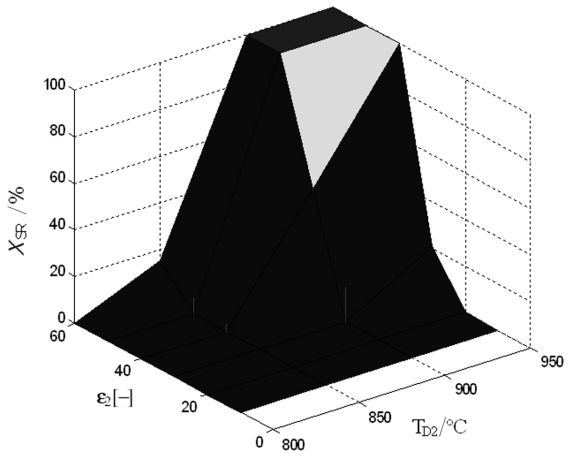

Figure 7: Comparasion of measurement and calculated values for equation
Slika 7: Primerjava meritev in izračunov z enačbo (6)

where:
ε/% is the relative deformation,
Z/s^{-1} is Zener-Holomon's parameter,
$B0$ = 0.4913
$B1$ = –0.6347
$B2$ = 0.07653

Equation (6) was deduced for describing the dependence share of the recrystallisation versus the extent of the deformation and the temperature

$$X_{SR} = 100 \cdot \left\{ 1 - e^{\left[a_1 (\varepsilon_2 - 0.1)^{a_2} (T_{D2} - 800)^{a_3} \right]} \right\} \qquad (6)$$

where:
X_{SR}/% is the amount of statically recrystallised austenite,
ε_2/% is the relative deformation,
T_{D2} /°C is the second deformation temperature,
$a1$= –3.49·10^{-22}
$a2$ = 18.1048
$a3$ = 15.38

A graphical comparison of the calculated and measured values is shown in **Figure 7**.

4 CONCLUSION

We performed experiments to investigate the effect of changes of the final deformation and deformation temperature on the austenite grain size and on the share of static austenite recrystallisation. From the results of these experiments the conditions necessary to design the technology for crankshaft smith forging were established:

the best conditions leading to a completely static recrystallisation of austenite (X_{SR} = 100 %) with forging are ε_2 = 50 and 60 % at $T_{\varepsilon 2}$ = 900 °C and 950 °C.

In these conditions an austenite grain size of $d_{\gamma 2}$ = 7.7–11.0 µm is achieved,

- acceptable conditions leading to the static recrystallization of austenite (X_{SR} = 90 %) are ε_2 = 40 % at $T_{\varepsilon 2}$ = 950 °C, which ensure an austenite grain size of $d_{\gamma 2}$ = 10 µm;
- with the application of numerical statistical methods for the processing of experimental data, equations for the influence of temperature on the extent of the deformations on the size of the austenite grains were derived, together with the austenite static recrystallization.

Acknowledgements

The authors acknowledge the support given by the EUREKA E!3192 ENSTEEL.

5 REFERENCES

[1] Feldmüller, A., Kern, T. U.: Design and materials for modern steam power plants an actual concept, In: PARSONS 2000 Advanced materials for 21st century turbines and power plant, 2000, Proceedings of the fifth international Charles Parsons turbine conference, 2000, 143–156

[2] Sedmak, A., Sedmak, S.: Critical crack assessment procedure for high pressure steam turbine rotors, In: Fatigue Fract Eng Mater Struct 18 (**1995**), 23–24

[3] Jing JianPing, Meng Guang, Sun Yi, Xia SongBo: An effective continuum damage mechanics model for creep–fatigue life assessment of a steam turbine rotor: International Journal of Pressure Vessels and Piping 80 (**2003**), 389–396

[4] Abe, F., Igarashi, M., Fujitsuna, N., Kimura, K., Muneki S.: Materials for advanced power engineering, In: Proceedings of sixth liege conference, Materials for advanced power engineering, Ibid 1, 1998, 259

[5] Kimura, K., Kushima, H., Abe, F., Yagi, K., Irie, H.: Assessment of creep strength properties of 9 to 12 % steels from a viewpoint of inherent creep strength, In: Advances in turbine materials, design and manufacturing, Proceedings of fourth international Charles Parsons turbine conference, 1997, 257–269

[6] Masuyama, F., Nishimura, N.: Strength of materials, In: The Japan Institute Metals, Advanced materials and technologies 2 (**1994**), 204

UDK 678:620.172
Original scientific article/Izvirni znanstveni članek

ISSN 1580-2949
MTAEC9, 42(3)125(2008)

THE OFF-AXIS BEHAVIOR OF A UNIDIRECTIONAL FIBER-REINFORCED PLASTIC COMPOSITE

ZUNAJOSNO OBNAŠANJE ENOSMERNIH Z VLAKNI OJAČENIH PLASTIČNIH KOMPOZITOV

Tomáš Kroupa, Vladislav Laš

University of West Bohemia in Pilsen, Department of Mechanics, Univerzitní 22, 306 14, Plzeň, Czech Republic
kroupa@kme.zcu.cz

Prejem rokopisa – received: 2007-09-20; sprejem za objavo – accepted for publication: 2008-01-10

Numerical and experimental investigations of the off-axis behavior of a unidirectional fiber-reinforced plastic composite consisting of carbon fibers and an epoxy matrix are presented. Static tensile tests of thin carbon-epoxy composite strips with various fiber directions were performed and simulated using a finite-element program. Puck's action-plane concept (failure criterion) and progressive failure analysis were used for the damage prediction of the tested thin strips. A non-linear stress-strain relation was used for modeling the off-axis behavior. The relation between the tensile force and the displacement in the direction of the loading force and the ultimate tensile force, which caused damage and the ultimate displacement of specimens, were measured and compared with the results of the numerical simulation. The fiber directions of the specimens, measured from the direction of loading, were in the interval 0°–90°.

Good agreement between the experimental results and the numerical simulations was achieved. The non-linear stress-strain relation was verified for the case of a long-fiber carbon-epoxy composite loaded with a static tensile loading force.

Keywords: Composite, PFA, tensile, non-linear, carbon-epoxy, failure

Predstavljeni so rezultati laboratorijske in numerične raziskave zunajosnega obnašanja enosmernih laminatov iz ogljikovih vlaken in epoksi matice. Izvršeni so bili statični preizkusi tankih kompozitnih lamel z različno smerjo vlaken in simulirani z uporabo metode končnih elementov za napoved pojava poškodbe lamel. Pockov model vpliva (kriterij zloma) in progresivna analiza poškodbe sta bila uporabljena za napoved poškodbe preizkusnih tankih lamel. Nelinearen odnos napetost deformacija je bil uporabljen za modeliranje zunaj osnega obnašanja. Določeno je bilo razmerje med natezno silo in premikom v smeri obremenitve in končna natezna sila, ki je povzročila poškodbo ter končni premik in oboje je bilo primerjano z rezultati numerične simulacije. Kot med smerjo vlaken v vzorcih in med smerjo obremenitve je bil med 0° in 90°.

Doseženo je bilo dobro ujemanje med eksperimentalnimi rezultati in rezultati simulacije. Nelinearen odnos napetost deformacija je bil preverjen za primer dolgovlaknatih ogljik-epoksi kompozitov, obremenjenih s statično silo.

Ključne beside: Kompoziti, PFA, natezni preizkusi, nelinearnost, ogljik-epoksi, poškodba

1 INTRODUCTION

New types of materials such as fiber-reinforced plastic (FRP) composites are being used increasingly often. A common model for FRP composites is the transversely isotropic model. This model shows good agreement with experiments in cases when the shear stress (or stresses for the case of a full three-dimensional stress state) does not reach values comparable to the limit of the strength. Therefore, a non-linear stress-strain relation for the FRP composites was developed [1]; this takes into account the non-linear behavior of the shear stress in composite materials. It was developed many years ago, but it was not commonly used due to the computational requirements of the non-linear simulations. Also, it is very difficult – and in most cases impossible – to obtain analytical solutions with the use of a non-linear stress-strain relation. Now, however, computational power allows us to solve non-linear problems (mostly with the use of the FEM) in an acceptable time, even on conventional PC configurations, and so it would be useful to apply a more precise stress-strain relation for the modeling of composites. For this reason the verification of the non-linear stress-strain relation is necessary, and this is the main topic of the paper.

Several papers have already been published by this team of authors in the field of modeling unidirectional composite materials. The identification of the material constants and the failure analysis of unidirectional long-fiber carbon-epoxy composite materials loaded by pure tension force were already performed for three types of specimens (thin composite strips) with different dimensions and fiber directions, with angles 0°, 45° and 90° to the direction of the loading force. The results obtained with the use of the linear stress-strain relation were presented in [7] and [8]. The results obtained with the use of a non-linear stress-strain relation were presented in [4]. A failure analysis was also performed in the articles mentioned above. The so-called progressive failure analysis, with the use of Puck's action-plane concept (see [5] or [6]), was carried out in [7] and [8], and with the use of Puck's action-plane concept and LaRC04 [3] the failure criterion was investigated [4].

Once the material constants were identified for special fiber directions, the verification of the non-linear

stress-strain relation for a unidirectional long-fiber composite can be performed for arbitrary fiber directions.

Static tensile tests of thin, unidirectional carbon-epoxy strips with fiber directions of 0°, 15°, 30°, 45°, 60°, 75° and 90° were performed. The ultimate forces and the force-displacement diagrams were obtained and compared with the results of numerical analyses that were performed with the use of the MSC.Marc 2005r3 FEM software. The progressive failure analysis with the use of Puck's action-plane concept was used for the damage analysis of the strips. The non-linear stress-strain relation and the failure model were implemented in suitable subroutines.

2 NON-LINEAR STRESS-STRAIN RELATION

The linear stress-strain relation (the constitutive relation for a transverse isotropic material) for composite materials can be written in the form [2]

$$\begin{pmatrix} \sigma_{\mathrm{L}} \\ \sigma_{\mathrm{T}} \\ \tau_{\mathrm{LT}} \end{pmatrix} = \begin{pmatrix} C_{11} & C_{12} & 0 \\ C_{12} & C_{22} & 0 \\ 0 & 0 & C_{66} \end{pmatrix} \begin{pmatrix} \varepsilon_{\mathrm{L}} \\ \varepsilon_{\mathrm{T}} \\ \gamma_{\mathrm{LT}} \end{pmatrix} \quad (1)$$

where σ_{L} and σ_{T} are the normal stress in the fiber direction (index L – longitudinal) and the normal stress in the direction transverse to the fibers (index T – transverse), and τ_{LT} is the shear stress in the plane of the strip; ε_{L} and ε_{T} are the strains in the L, T directions and γ_{LT} is the shear strain in the plane of the layer and matrix C (with the elements C_{ij} dependent on the material constants) is the stiffness matrix.

This form of stress-strain relation is sufficient in cases when the shear stress does not reach values comparable to the limit of the strength. The non-linear behavior of the material is obvious in the latter cases.

Therefore, a non-linear stress-strain relation was developed [1]. It can be written in the form

$$\begin{pmatrix} \sigma_{\mathrm{L}} \\ \sigma_{\mathrm{T}} \\ \tau_{\mathrm{LT}} \end{pmatrix} = \begin{pmatrix} C_{11} & C_{12} & 0 \\ C_{12} & C_{22} & 0 \\ 0 & 0 & C_{66} \end{pmatrix} \begin{pmatrix} \varepsilon_{\mathrm{L}} \\ \varepsilon_{\mathrm{T}} \\ \gamma_{\mathrm{LT}} \end{pmatrix} + f(\gamma_{\mathrm{LT}}) \begin{pmatrix} 0 \\ 0 \\ \gamma_{\mathrm{LT}} \end{pmatrix} \quad (2)$$

where $f(\gamma_{\mathrm{LT}})$ is the only one real root of the cubic equation

$$y^3 + \frac{3}{S_{66}} y^2 + \left(\frac{3}{S_{66}^2} + \frac{S_{66}}{S_{6666}} \frac{1}{\gamma_{\mathrm{LT}}^2} \right) y + \frac{1}{S_{66}^3} = 0 \quad (3)$$

where S_{6666} is the so-called fourth-order compliance coefficient (additional material constant [Pa^{-3}]) and $S_{66} = 1/C_{66}$.

3 FAILURE ANALYSES

Failure criteria are used for the prediction of the composite material's failure. There are several types of failure criteria. Research has shown that a composite material can be damaged in several modes (matrix cracking, crushing, fiber cracking, and kinking). Therefore, direct mode criteria were developed (Hashin [3], the Puck action-plane concept [5,6] or LaRC04 [3]).

Puck's action-plane concept was chosen in this work to predict the failure of the examined strips. For a precise description of the criterion see [5] and [6].

The failure criteria are able to determine the first failure in the model. However, once the propagation of failure is investigated, a progressive failure analysis is needed. The flow chart of the progressive failure analysis (PFA) for a one time pseudo-increment is shown in **Figure 1**. If the failure is recognized in any element for the prescribed loading force, the stiffness matrix of the damaged elements is changed with a dependence on the type of failure (e.g., fiber or matrix). If the model does not contain any damaged elements the loading force increases and the next time pseudo-increment is solved. For further information about PFA see [8].

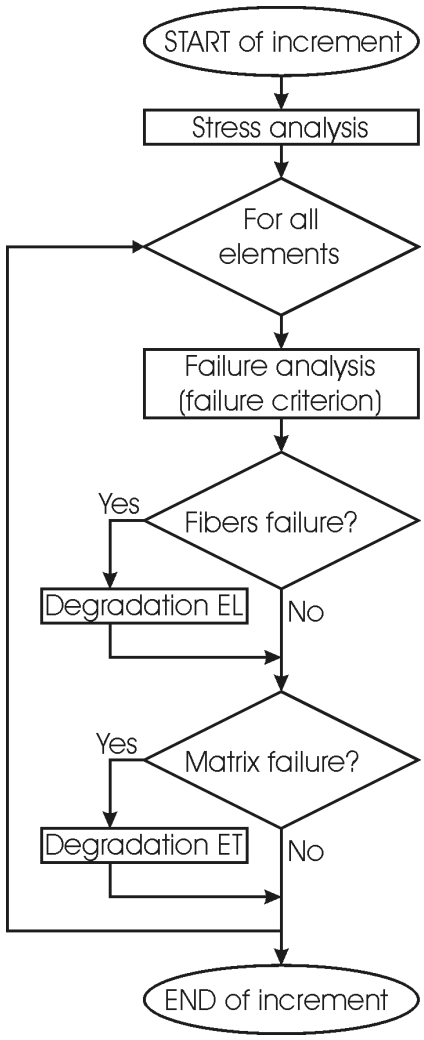

Figure 1: Flow chart of PFA
Slika 1: Potek FPA

4 EXPERIMENTS

The experimental specimens (thin strips) were cut with a water jet from a single, large, unidirectional plate. It was made from four pre-pregs using autoclave technology.

The dimensions of the specimens and the fiber angle and the direction of the loading force are shown in **Figure 2**. If the fiber direction is parallel to the direction of the loading force, the use of aluminum bandages is necessary in order to avoid crushing the specimen between the grips of the testing machine.

As mentioned above, several tests and analyses were already performed on similar types of material (i.e., carbon-epoxy). Previous experiments were performed on the same ZWICK/ROELL Z050 test machine as that used for the experiments in the present work. The set of material constants shown in **Table 1** was identified in [4].

Table 1: Previously identified material constants for similar material
Tabela l: Prej določene konstante za podoben material

Stiffness and Poisson's ratio	
E_L	109.4 GPa
E_T	7.7 GPa
G_{LT}	4.5 GPa
ν_{LT}	0.28
Fourth-order compliance coefficient	
S_{6666}	1.5×10^{-25} Pa^{-3}
Strength	
X^T	2128 MPa
X^C	1160 MPa
Y^T	44 MPa
Y^C	200 MPa
S^L	52 MPa

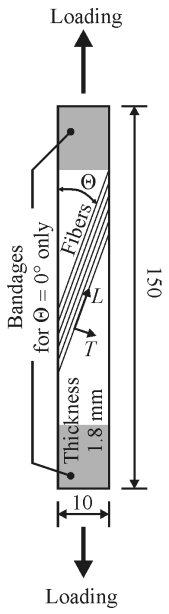

Figure 2: Strips
Slika 2: Preizkusna lamela

In the present work, the experiments were performed for the fiber directions 0°, 15°, 30°, 45°, 60°, 75° and 90°. Ten specimens were tested for each of the fiber directions.

5 RESULTS

The specimens used in the experiments were cut from the plate made from pre-pregs with different thicknesses than the plate used in [4,7,8], and also with slightly different material constants. It is obvious from **Tables 1 and 2** that the fourth-order compliance coefficient S_{6666} is now two times smaller, and that the tensile strength in the transverse direction Y^T and the shear strength S^L are slightly different.

Table 2: Material constants
Tabela 2: Konstante materiala

Stiffness and Poisson's ratio	
E_L	109.4 GPa
E_T	7.7 GPa
G_{LT}	4.5 GPa
ν_{LT}	0.28
Fourth-order compliance coefficient	
S_{6666}	0.75×10^{-25} Pa^{-3}
Strength	
X^T	2128 MPa
X^C	1160 MPa
Y^T	38 MPa
Y^C	200 MPa
S^L	62 MPa

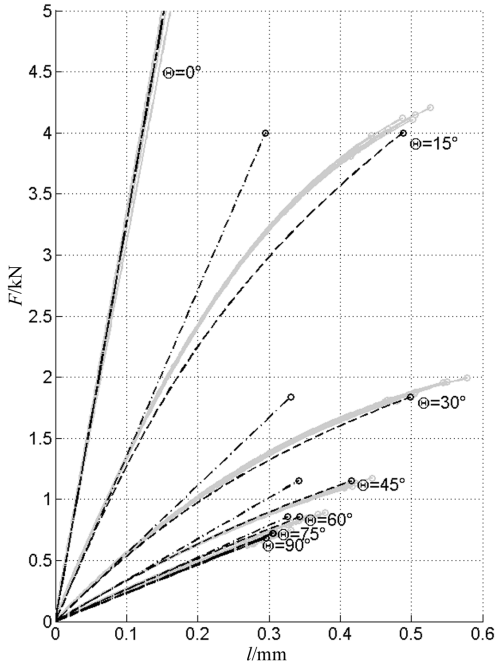

Figure 3: Force-displacement diagram (gray – experiment, dashed – FEM non-linear, dash-and-dot – FEM linear)
Slika 3: Diagram sila-premik (sivo – eksperiment, črtkano – FEM nelinerano, črtno-točkasto– FEM linearno)

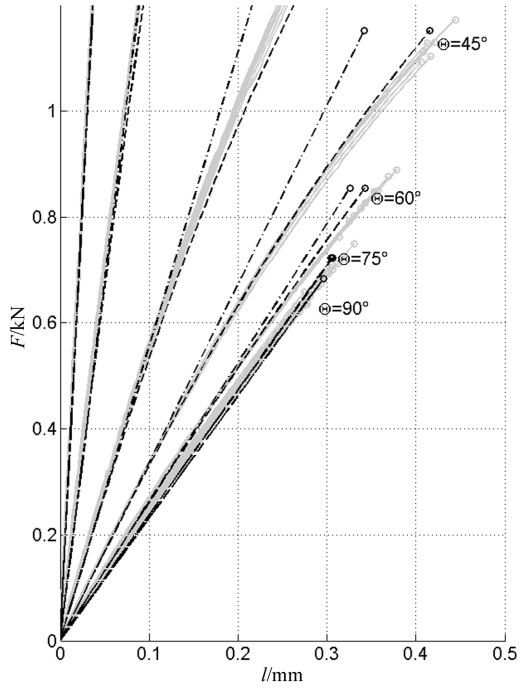

Figure 4: Force-displacement diagram (gray – experiment, dashed – FEM non-linear, dash-and-dot – FEM linear)
Slika 4: Diagram sila-premik (sivo – eksperiment, črtkano – FEM nelinearno, črtnotočkasto- FEM linearno)

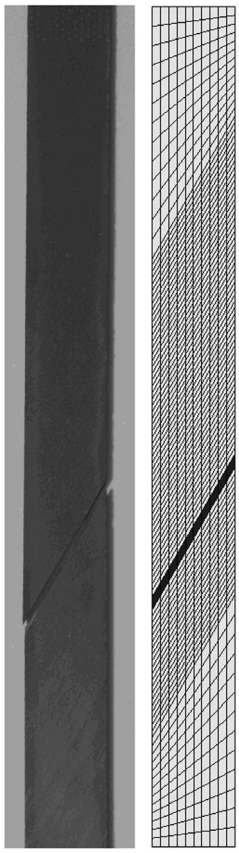

Figure 5: Damaged strip (left – photograph of specimen, right – FEM model)
Slika 5: Poškodovana lamela (levo – lamela, desno – FEM model)

Figure 3 and **Figure 4** show force-displacement diagrams for all of the measured fiber angles.

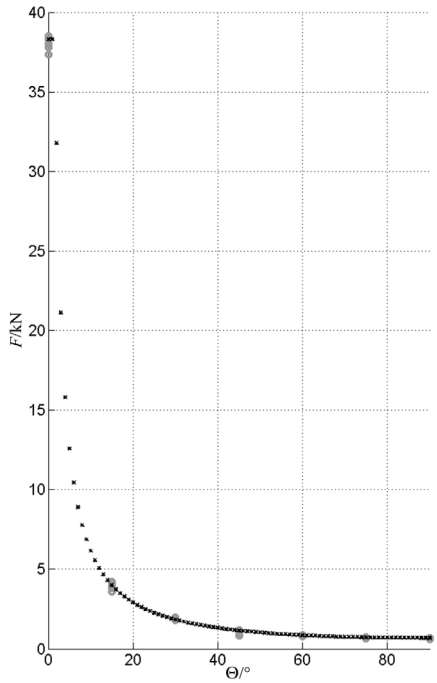

Figure 6: Ultimate force as a function of fiber angle Θ (gray circle – experiment, black dot and cross – linear and non-linear FEM)
Slika 6: Končna sila v odvisnosti od kota vlaken Θ (sivi krogci – eksperiment, črne točke in križci – linearni in nelinearni FEM)

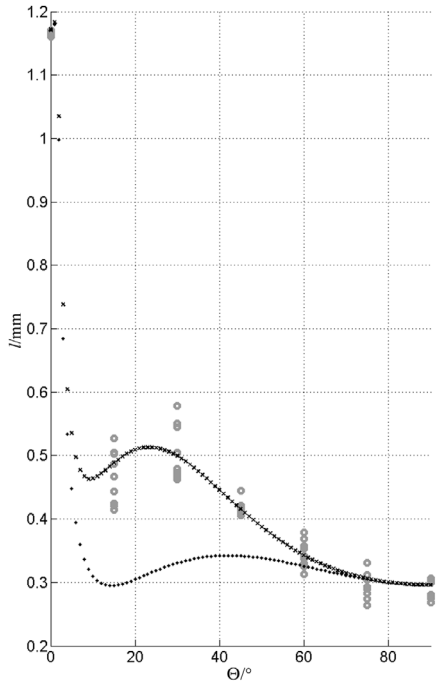

Figure 7: Ultimate displacement of the strips as a function of the fiber angle Θ (gray circle – experiment, cross – non-linear FEM, dot – linear FEM)
Slika 7: Končni premik lamel v odvisnosti in kota vlaken Θ (sivi krogci – eksperiment, križci – nelinearni FEM, točke – linearni FEM)

Figure 5 shows the damaged strip with a fiber angle of $\Theta = 30°$. On the left-hand side is the real damaged material, and on the right-hand side is the damaged FEM model (the black elements are damaged – tensile failure mode of matrix). Figure 6 shows the ultimate force as a function of the fiber angle.

As shown in **Figure 6**, the ultimate tensile force is a strictly decreasing function of the fiber angle. In contrast to this, the ultimate displacement of the strips is not. As shown in **Figure 7**, there is a local maximum of the function around $\Theta = 23°$. The difference between the linear and the non-linear stress-strain relation is obvious from **Figure 7**.

6 CONCLUSION

The non-linear stress-strain relation was verified by a simple tensile test for the case of a unidirectional long-fiber carbon-epoxy composite for the full range of fiber angles, 0°–90°.

The numerical analyses were preformed with the use of non-linear and linear stress-strain relations in order to compare the influence of nonlinearity. The numerical analysis combining the non-linear stress-strain relation with the progressive failure analysis using Puck's action-plane concept shows good agreement with the experiments.

Further research will focus on the non-linear behavior of laminated composites.

Acknowledgements: The work has been supported by the grant projects GA AS CR no. A200760611 and GACR no. 101/07/P059.

7 REFERENCES

[1] H. T. Hahn, W. S. Tsai, Nonlinear Elastic Behavior of Unidirectional Composite Laminae, Journal of Composite Materials, 7 (**1973**), 102–118

[2] J. M. Berthelot, Composite materials, Springer, New York 2004, 639

[3] T. P. Silvestre, G. C. Dávila, P. P. Camanho, L. Iannucci, O. Robinson, Failure models and criteria for FRP under in-plane or three-dimensional stress state including shear non-linearity, Research report, NASA/TM-2005-213530, NASA Langley research center VA 23681 USA, 2005

[4] T. Kroupa, R. Zemčík, V. Laš, Identification of composite material properties using non-linear stress-strain relation, Proc. of the Applied Mechanics, Srní, CR, 2006

[5] A. Puck, J. Kopp, M. Knops, Guidelines for the determination of the parameters in Puck's action plane strength criterion, Composite Science and Technology 62 (**2002**), 371–378

[6] A. Puck, H. Schürmann, Failure analysis of FRP laminates by means of physically based phenomenological models. Composite Science and Technology, 58 (**1998**), 1045–1067

[7] R. Zemčík, V. Laš, Identification of composite material properties using progressive failure analysis, Proc. of the Computational Mechanics, Nečtiny, CR, 2005

[8] R. Zemčík, V. Laš, Numerical simulation of damage in fiber-reinforced composites and comparison with experiment, Proc. of the 22nd DANUBIA–ADRIA Symposium on Experimental Methods in Solid Mechanics, Monticelli Terme, IT, 2005

UDK 669.1:669.784:620.193.1
Professional article/Strokovni članek

ISSN 1580-2949
MTAEC9, 42(3)131(2008)

THE INFLUENCE OF CARBON CONTENT ON THE CORROSION OF MGO-C REFRACTORY MATERIAL CAUSED BY ACID AND ALKALINE LADLE SLAG

VPLIV VSEBNOSTI OGLJIKA NA KOROZIJO OGNJEVZDRŽNEGA MATERIALA MGO-C V KISLI IN BAZIČNI PEČNI ŽLINDRI

Zdenčk Adolf, Petr Suchánek, Ivo Husar

VŠB-Technical University of Ostrava, Faculty of Metallurgy and Materials Engineering
17. listopadu 15/2172, 708 33 Ostrava-Poruba, Czech Republic
zdenek.adolf@vsb.cz

Prejem rokopisa – received: 2007-10-08; sprejem za objavo – accepted for publication: 2007-11-15

This paper describes an investigation of the influence of increasing carbon content on the corrosion of MgO-C refractory material by molten slag. The refractory material contained mass fraction of 98 % MgO, approximately 2 % Fe_2O_3, and graded quantities from 3 % to 18 % C. The corrosion was investigated in melts of reduction ladle slags at a temperature of 1600 °C in laboratory conditions. A sample of refractory material with dimensions of 10 × 10 × 100 mm was submerged into the molten slag and exposed to the corrosive effect of the slag for 60 min. After the expose of the refractory material the slag was cooled down and submitted to a chemical analysis. After a comparison of the MgO content in the slag before and after the corrosion test the amount of MgO content in the melt was determined and the degree of corrosion of the refractory material was quantified. The experiments were realised using final slags from the ladle furnace (LF), strongly alkaline slag $w(CaO)/w(SiO_2) = 4.43$, and also acidic slags $w(CaO)/w(SiO_2) = 0.94$ with different contents of CaF_2. The work was carried out within the frame of the projects EUREKA E!3580 and IMPULS FI-IM4/110.

Keywords: MgO-C refractory material, corrosion of refractory material, ladle slag

V članku so predstavljene raziskave vpliva naraščanja vsebnosti ogljika na korozijo MgO v raztaljeni žlindri. Ognjevzdržni material je imel masni delež 98 % MgO, okoli 2 % Fe_2O_3 in od 3 % do 18 % C. Kororzija je bila raziskana v laboratoriju v redukcijskih žlindrah pri temperaturi okoli 1600 °C. Vzorec ognjevzdržnega materiala z velikostjo 10 x 10 x 100 mm je bil potopljen 60 min. v žlindro, nato je bila žindra ohlajena in analizirana. S primerjavo vsebnosti MgO pred preskusom korozije in po njem, je bila opredeljena intenziteta korozije. Za preizkuse smo uporabili končno žlindro iz ponovčne peči (LF): močno bazično žlindro $w(CaO)/w(SiO_2) = 4.43$ in kislo žlindro $w(CaO)/w(SiO_2) = 0.94$ z različnimi dodatki CaF_2: Raziskava je bila izvršena v okviru projektov EUREKA E!3580 in IMPULS FI-IM4/110.

Ključne besede: ognjevarni material MgO-C, korozija ognjevarnega materiala, ponovčna žlindra

RESULTS

The chemical composition of the slags before the exposure is given in the **Table 1**.

Table 1 shows that the acidic slag contains very little of the CaF_2 (w = 0.82 %), and that the alkaline slag contains 7.18 % CaF_2, added to increase its fluidity.

The MgO content of the slags after exposure to the refractory material is shown in **Tables 2 and 3**. The tables also contain increments of the MgO content and the increments related to the initial MgO content in the slags (η_{MgO}). The six tested samples of refractory material differed only in terms of the carbon content, graded from 3 % to 18 %. However, sample 5 % contained 15 % C in addition to an antioxidant.

Figures 1 and 2 show the change of the MgO content in slags with respect to the carbon content in the refractory material.

In order to enable a comparison of the quantitative effect of carbon content in the MgO-C refractory material on its corrosion intensity by acidic and alkaline slag, the changes in the MgO and carbon contents in **Tables 1 and 2** were transformed according to Equations (1) and (2).

$$\bar{x}_i = \frac{x_i - x_{\min}}{x_{\max} - x_{\min}} \quad (1)$$

Table 1: Chemical composition and alkalinity of the slags used for the corrosion test
Tabela 1: Kemična sestava in bazičnost žlinder, ki sta bili uporabljeni za preizkuse korozije

Slag	Σ Fe	SiO_2	Al_2O_3	CaO	MgO	CaF_2	B1	B2
	(w/%)						(1)	
acidic	1.58	41.1	7.0	38.8	8.0	0.82	0.94	0.80
alkaline	0.75	13.7	13.5	60.7	5.6	7.18	4.43	2.23
$B_1 = \frac{w(CaO)}{w(SiO_2)}$				$B_2 = \frac{w(CaO)}{w(SiO_2) + w(Al_2O_3)}$				

Table 2: Changes to the MgO content in an acidic slag for different carbon contents in the refractory material
Tabela 2: Spremembe vsebnosti MgO v kisli žlindri pri različni vsebnosti ogljika v ognjevzdržnem materialu

Refractory material	ACIDIC SLAG				
	Carbon contents, w(C)/%	w(MgO)/%			η_{MgO}/%
		Before the corrosion test	After the corrosion test	w(ΔMgO)	
1	3	8.0	19.8	11.8	147.5
2	6		14.0	6.0	75.0
3	10		15.0	7.0	87.5
4	15		12.5	4.5	56.3
5	15 + antioxidant		12.8	4.8	60.0
6	18		12.1	4.1	51.2
$\eta_{MgO} = \frac{w(MgO)_{po} - w(MgO)_{pred}}{w(MgO)_{pred}} \cdot 100\%$					

Table 3: Changes to the MgO contents in an alkaline slag for different carbon contents in the refractory material
Tabela 3: Spremembe vsebnosti MgO v bazični žlindri pri različni vsebnosti ogljika v ognjevzdržnem materialu

Refractory material	ALKALINE SLAG				
	Carbon contents, w(C)/%	w(MgO)/%			η_{MgO}/%
		Before the corrosion test	After the corrosion test	w(ΔMgO)/%	
1	3	5.6	9.7	4.1	73.2
2	6		7.1	1.5	26.8
3	10		6.2	0.6	10.7
4	15		6.3	0.7	12.5
5	15 + antioxidant		6.3	0.7	12.5
6	18		6.7	1.1	19.6

$$\bar{y}_i = \frac{y_i - y_{min}}{y_{max} - y_{min}} \quad (2)$$

where:

$\bar{x}_i$ is the transformed form of the independent variable of the quantity lg w(C), 1

$\bar{y}_i$ is the transformed form of the dependent variable of the quantity lg w(ΔMgO), 1

x_i is the concrete value of the independent variable of the quantity lg w(C), 1

y_i is the concrete value of the dependent variable of the quantity lg w(ΔMgO), 1

x_{max}; x_{min}, y_{max}; y_{min} are the maximum or minimum values of the variable quantities lg w(C) and lg w(ΔMgO), 1

The quantities thus transformed were analysed with linear regression and the equations of the straight lines, shown in **Figures 3 and 4**, were obtained.

Figures 3 and 4 indicate that the similarities of the dependencies expressed by the correlation coefficient are, in both cases, close, and the value of P is even lower

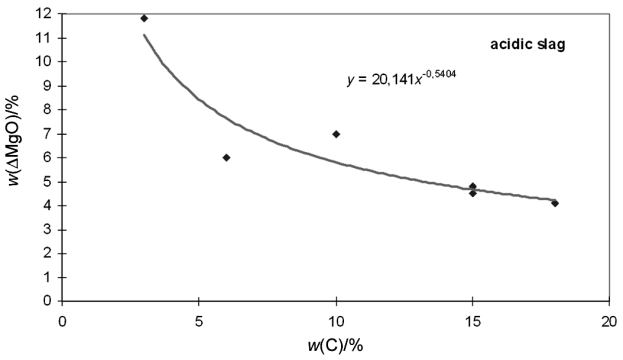

R	0.86	Reliability value R	0.735002	Value P	0.029083

Figure 1: Change in the content of MgO in acidic slag with respect to the carbon content in the refractory material
Slika 1: Spremembe vsebnosti MgO v kisli žlindri v odvisnosti od vsebnosti ogljika v ognjevzdržnem materialu

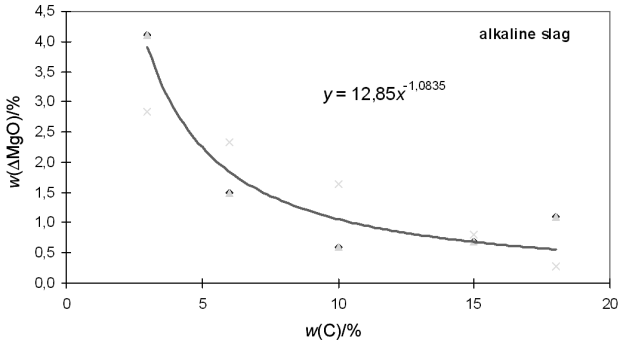

R	0.74	Reliability value R	0.549185	Value P	0.091887

Figure 2: Change in the content of MgO in the alkaline slag with respect to the carbon content in the refractory material
Slika 2: Spremembe vsebnosti MgP v bazični žlindri v odvisnosti od vsebnosti ogljika v ognjevzdržnem materialu

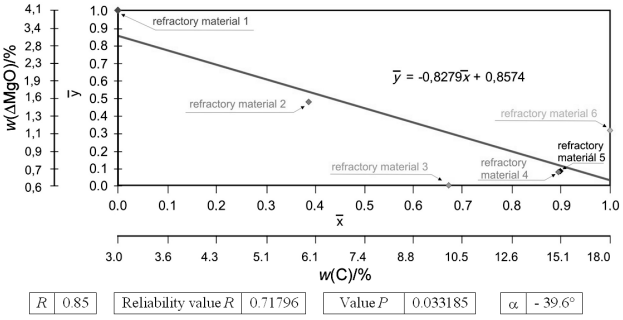

Figure 3: Dependence of w (ΔMgO) in the acidic slag on the carbon contents in refractory material after linear regression of the experimental data

Slika 3: Odvisnost ΔMgO v kisli žlindri pri različni vsebnosti ogljika v ognjevzdržnem materialu, linearna regresija eksperimentalnih rezultatov

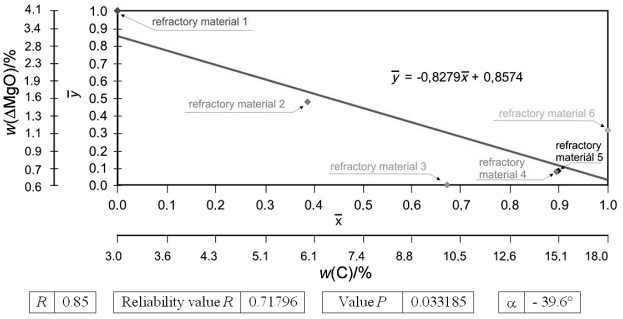

Figure 4: Dependence of w(ΔMgO) in the alkaline slag on the carbon contents in refractory material – evaluated by linear regression of the experimental data

Slika 4: Odvisnost ΔMgO v bazični žlindri pri različni vsebnosti ogljika v ognjevzdržnem materialu, linearna regresija eksperimentalnih rezultatov

than 0.05. The value P indicates the statistical significance of the tested factor. A value of $P < 0.05$ means that the tested factor has a statistically significant impact on the values of the given parameter. The effect of increasing the carbon content on reducing the wear of the MgO-C refractory material is significant for both types of slags – this is clearly evident from the slope of the straight line and the corresponding angle α, which approaches 45°. For the acidic slag the scatter of the values is smaller and the slope of the dependence is greater.

CONCLUSIONS

The acidic slag (B_1 = 0.94) dissolves a great deal more MgO-C refractory material, i.e., within the range 4.1–11.8 % MgO. The relative change of the MgO content in the slag is in the range η_{MgO} = 51.2–147.5 %.

The alkaline slag (B_1 = 4.43) dissolves significantly less MgO-C refractory material, i.e., within the range 0.6–4.1 % MgO, and the relative change of the MgO content is η_{MgO} = 10.7–73.2 %

The favourable effect of carbon in MgO-C refractory material on delaying the corrosion is stronger, particularly above 10 % C, for both slags, but more in the acidic slags with low contents of easily reducible oxides.

The dependence w(ΔMgO) = $f(w(C))$ is hyperbolic and shows a good correlation with the experimental data.

The possible effect of an antioxidant was not detected, probably because the tests were performed with reduction ladle slags.

LITERATURE

[1] Suchánek, P., Adolf, Z., Salva, O., Husar, I. Vliv chemického složení pánvových strusek na korozi žáromateriálu vyzdívky pánvové pece. (Chemical Composition Effect of Ladle Slag on Refractory Corrosion of Ladle Furnace Lining). In Teorie a praxe výroby a zpracování oceli. 23. celostátní konference se zahraniční účastí, Rožnov pod Radhoštěm, 3.–4. dubna 2007, © TANGER s.r.o. Ostrava, 141–149. ISBN 978-80-86840-32-1

[1] Adolf, Z., Suchánek, P., Husar, I., Salva, O. Koroze MgO-C žáromateriálu pánvovými struskami. (Ladle Slag Corrosion of MgO-C Refractory). In Nowe technologie i materiały w metalurgii i inzynierii materiałowej. XV Seminarium Naukowe, Katowice, 18 maja 2007, 43–46 (ISBN 83:978-83-910722-9-0)

UDK 669.14.018:621.73:621.438
Professional article/Strokovni članek

ISSN 1580-2949
MTAEC9, 42(3)135(2008)

AN EVALUATION OF THE PROPERTIES OF ROTOR FORGINGS MADE FROM 26NiCrMoV115 STEEL

OCENA LASTNOSTI IZKOVKOV ZA ROTORJE IZ JEKLA 26NiCrMoV115

Martin Balcar[1], Václav Turecký[1], Libor Sochor[1], Pavel Fila[1], Ludvík Martínek[1], Jiří Bažan[2], Stanislav Němeček[3], Dušan Kešner[3]

[1]ŽĎAS, a. s., Strojirerska 6, 59171 Žďár nad Sázavou, Czech Republic
[2]VŠB TU – Ostrava, Czech Republic
[3]COMTES FHT, s .r. o. Plzeň, Czech Republic
martin.balcar@zdas.cz

Prejem rokopisa – received: 2007-09-26; sprejem za objavo – accepted for publication: 2007-10-15

The development and verification of production technology for the rotor forgings of compressors and generators demonstrate the significant effect of the forming of the input ingot on the final properties of the forgings.

The measured yield strength and the strength limit show a trend of dependence on the sample's position in the rotor. Significant differences in the longitudinal as well as in the transversal directions over the cross-section of a forging have been found, especially for the transition temperature FATT T_{50}. The mechanical properties of experimental rotor forgings made of 26NiCrMoV115 steel indicate that the forming and heat-treatment processes can be optimized.

Keywords: gas turbine, rotor shaft, forging, mechanical properties, FATT T_{50}

Razvoj tehnologije za preverjanje izdelave rotorskih izkovkov za kompresorje in generatorje kaže na zelo pomemben vpliv preoblikovanja izhodnega ingota na dosežene lastnosti izkovka. Meja plastičnosti in trdnost sta odvisni od položaja vzorca v rotorju. Ugotavljene so bile pomembne razlike med podolžno in prečno smerjo na prerezu rotorja, posebno pri prehodni temperaturi FATT T_{50}. Mehanske lastnosti eksperimentalnih izkovkov za rotorje iz jekla 26NiCrV 115 kažejo, da bi bilo mogoče optimizirati procesa kovanja in toplotne obdelave.

Ključne besede. plinska turbina, rotorska gred, kovanje, mehanske lastnosti, FATT T_{50}

The investigations were performed within the EUREKA program of the E!3192 ENSTEEL project, identification number 1P04EO169. The project was funded partially with the financial support of the Ministry of Education, Youth and Sport of the Czech Republic.

1 INTRODUCTION

The manufacturing of rotors for gas-turbine compressors and generators, applying the technology in the company ŽĎAS, a. s., Czech Republic, was verified from the viewpoint of the obtained in-service properties of the product.

Three experimental heats were produced (EU1, EU2 and EU3) from the steel grade 26NiCrMoV115. The 8K10.0 ingots were cast and the rotor forgings were forged to the shape shown in **Figure 1**. After the basic heat treatment of the forgings, consisting of water quenching from 850 °C, tempering at 615 °C and a cooling rate of 25 °C/h down to 250 °C, followed by air cooling, the mechanical properties on the forging's cross-section were determined.

The following places were chosen for determining the mechanical properties of the final forging: (B) – bottom, (C) – centre, (H) – head. These correspond to the same positions in the original ingot.

The properties were determined with tensile tests (THZ 723), toughness tests (PSW 300 and AMSLER TV 742) and Brinell hardness measurements (KPE 3000).

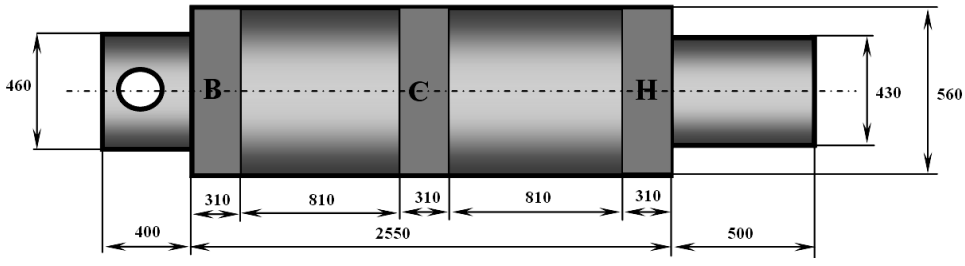

Figure 1: Layout of the experimental piece of the forging and the places from where the samples were taken
Slika 1: Položaj izrezov iz izkovka in mesta odvzema vzorcev

In **Table 1** the requirements for the mechanical properties of the rotors for the compressor and generator are given according to the customer's specification.

The heat-treatment conditions for the compressor rotors were chosen for the experimental tests. It was assumed that it would be possible to obtain the required yield strength and tensile strength for the mechanical properties of the generator's rotor by increasing the tempering temperature.

It is also worth noting that the forging dimensions at the place where the sample is taken for a determination of the mechanical properties do not exceed a diameter of 250 mm or a wall thickness of 200 mm. The test forgings were semi-products designated for the determination of the impact of forming and the heat treatment on the obtained service properties of the material during the fabrication of forgings with a large cross-section.

2 TENSILE TEST AT ROOM TEMPERATURE

Table 2 summarises the tensile properties determined in the longitudinal direction at room temperature (20 °C). The values obtained with the specimen cut at the forging surface that are not highlighted do not fulfil the required values for the mechanical properties of the compressor rotor.

It is clear from **Table 2** that the required yield point was not achieved in the heat EU1 at the surface of the

Table 1: Requirements of the mechanical properties of forgings for the 26NiCrMoV115 steel
Table 1: Zahtevane mehanske lastnosti izkovkov iz jekla 26CrNiMoV115

26NiCrMoV115	Position of test		Mechanical properties (20°C)						
			$R_{p\,0.2}$	Rm	Elongation	Reduction of area	Charpy KV	Ductile fracture	FATT T_{50}
			($N.mm^{-2}$)	($N.mm^{-2}$)	(%)	(%)	(J)	(%)	(°C)
Compressor rotor	longitudinal	surface	800 to 900	≤ 1080	≥ 14	≥ 45	≥ 90	100	-
Generator rotor	longitudinal	axis	700 to 800	≤ 960	≥ 16	≥ 50	≥ 80	100	-
	longitudinal	surface	700 to 800	≤ 960	≥ 17	≥ 55	≥ 100	100	-
	transversal	surface	700 to 800	≤ 960	≥ 16	≥ 50	≥ 90	100	-40

Table 2: Mechanical properties at room temperature – longitudinal direction
Table 2: Mehanske lastnosti pri sobni temperatruri – vzdolžna smer

Longitudinal direction		$Rp_{0.2}$ MPa			Rm MPa			Elongation %			Reduction of area %		
		surface	1/2R	axis	surface	1/2R	axis	surface	1/2R	axis	surface	1/2R	axis
EU1	H	795	781	**829**	**955**	928	**927**	**17.4**	17.4	**14.8**	**65.2**	59.0	**43.8**
EU2	H	**877**	811	**836**	**1005**	939	**939**	**15.8**	16.0	**14.6**	**65.2**	52.4	**51.0**
EU3	H	**848**	809	**830**	**968**	928	**941**	**17.4**	16.2	**16.8**	**66.4**	56.4	**53.8**
EU1	C	793	826	**796**	**966**	931	**943**	**16.8**	16.4	**15.0**	**65.2**	53.8	**53.8**
EU2	C	**817**	786	**780**	**934**	899	**917**	**17.2**	14.0	**15.8**	**65.2**	**31.1**	**55.1**
EU3	C	**812**	791	**788**	**934**	915	**921**	**17.2**	18.0	**16.2**	**64.0**	56.4	**56.4**
EU1	B	**867**	806	**823**	**992**	926	**933**	**17.2**	15.4	**13.4**	**67.5**	52.4	**53.8**
EU2	B	**810**	778	**789**	**912**	881	**868**	**17.8**	15.4	**14.8**	**67.5**	52.4	**45.2**
EU3	B	**822**	783	**811**	**927**	895	**903**	**17.0**	17.0	**15.0**	**66.4**	56.4	**55.1**

Table 3: Mechanical properties at room temperature – transversal direction
Table 3: Mehanske lastnosti pri sobni temperaruri – prečna smer

Transversal direction		$Rp_{0.2}$ MPa			Rm MPa			Elongation %			Reduction of area %		
		surface	1/2R	axis	surface	1/2R	axis	surface	1/2R	axis	surface	1/2R	axis
EU1	H	**863**	797	820	**963**	923	926	14.6	**15.6**	14.8	**66.4**	60.3	60.3
EU2	H	**818**	803	796	**927**	920	927	**15.6**	16.8	16.6	**64.0**	62.8	60.3
EU3	H	**821**	787	833	**982**	933	939	**17.8**	16.2	17.0	**69.8**	61.6	61.6
EU1	C	**810**	803	816	**920**	913	940	14.6	**15.2**	**15.4**	**66.4**	59.0	59.0
EU2	C	790	772	784	**905**	894	903	**16.6**	**15.2**	13.8	**64.0**	57.8	56.4
EU3	C	**814**	794	791	**925**	912	920	**18.6**	17.2	16.4	**69.8**	61.6	60.3
EU1	B	**828**	818	820	**936**	938	945	**17.2**	**15.6**	16.6	**61.8**	60.3	59.0
EU2	B	765	754	779	**889**	894	892	**16.6**	16.4	13.8	**60.3**	56.4	51.0
EU3	B	**803**	779	795	**918**	909	917	**17.2**	17.4	16.4	**68.6**	59.0	61.6

Table 4: Mechanical properties at room temperature – average of heats EU1 – 3
Table 4: Mehanske lastnosti pri sobni temperaturi – povprečje talin EU1 – 3

Direction of testing	$Rp_{0.2}$ MPa			Rm MPa			Elongation %			Reduction of area %		
	surface	1/2R	axis	surface	1/2R	axis	surface	1/2R	axis	surface	1/2R	axis
Longitudinal	827	797	809	955	916	921	17.1	16.2	15.2	65.8	52.3	52.0
Transversal	812	790	804	929	915	923	16.5	16.2	15.6	65.7	59.9	58.8

Table 5: *KV* (J) and share of ductile fracture – DF (%) at room temperature
Table 5: *KV* (J) in delež duktilnega preloma – *DF* (%) pri sobni temperaturi

Transversal direction		Surface KV J	Surface *DF* %	1/2 R KV J	1/2 R *DF* %	Axis KV J	Axis *DF* %
EU1	H	118	*100*	48	*47*	91	*83*
EU2	H	130	*100*	45	*43*	68	*63*
EU3	H	144	99	39	*33*	59	*57*
EU1	C	120	*100*	48	*45*	51	*53*
EU2	C	106	*90*	40	*42*	50	*48*
EU3	C	147	*100*	34	*28*	56	*50*
EU1	B	113	*100*	36	*38*	68	*62*
EU2	B	143	*100*	55	*50*	68	*57*
EU3	B	151	*100*	43	*28*	70	*55*

Longitudinal direction		Surface KV J	Surface *DF* %	1/2 R KV J	1/2 R *DF* %	Axis KV J	Axis *DF* %
EU1	H	92	*98*	32	*35*	45	*51*
EU2	H	*80*	*83*	33	*32*	42	*45*
EU3	H	136	*98*	33	*22*	44	*35*
EU1	C	103	*98*	28	*28*	32	*35*
EU2	C	97	*88*	36	*28*	36	*40*
EU3	C	99	*83*	34	*22*	37	*33*
EU1	B	90	97	36	*35*	31	*31*
EU2	B	*85*	*90*	35	*38*	37	*38*
EU3	B	99	*83*	39	*30*	39	*28*

forging from the part of the body under the head and in the central part of the original ingot. Other mechanical properties satisfy the requirements for the compressor rotor in accordance with **Table 1**.

Table 3 shows the values of the mechanical properties determined by a tensile test in the transversal direction with the highlighted values of $R_{p0.2} < 800$ MPa.

Table 4 shows the average values of the mechanical properties determined by tensile tests of the forgings from ingots cast from the heats EU1, EU2 and EU3.

It is clear from the average values in **Table 4** that the mechanical properties in the longitudinal and transversal directions are comparable. However, the tensile strength is higher in the longitudinal direction.

3 THE NOTCH TOUGHNESS AND TRANSITION TEMPERATURE

The results of the measurement of notch toughness at room temperature in the longitudinal direction given by the change of the peak load *KV* (J) and the share of the ductile fracture (%) in terms of the position of taking the sample from the forging are given in **Table 5**.

The average values of three measurements on samples cut out at the forging surface in the longitudinal direction that do not satisfy the requirement *KV* = 90 J or share a portion of 100% ductile fracture (DF) are highlighted.

It is apparent from **Table 5** that the values satisfying the peak load in the transversal direction at the surface part of the forging were achieved, and only in two cases were areas of brittle fracture found on the ductile fracture surface. Comparatively low levels of peak load were achieved in the longitudinal direction, and in all cases the share of brittle fracture on the fracture surface was less than 20 %.

It can be concluded from these experimental results, especially from the share of the ductile fracture, that the required peak load values can be obtained with the existing technology of heat treatment only for small cross-sections.

Table 6: *KV* (J) and share of ductile fracture *DF* (%) for a determination of the FATT T_{50}
Table 6: *KV* (J) in delež duktilnega preloma *DF* (%) pri sobni temperaturi za določitev FATT T_{50}

transversal direction	T	Surface KV	Surface *DF*	1/2 R KV	1/2 R *DF*	axis KV	axis *DF*
	°C	J	%	J	%	J	%
H	80			114	*100*	127	*100*
	60			102	*88*	121	*99*
	40			77	***67***	85	*78*
	20	130	*100*	44	***41***	73	***68***
	0	110	*83*	29	*23*	49	***48***
	-20	75	*62*	26	*13*	35	*18*
	-40	85	***67***				
	-60	60	***49***				
C	80			94	*88*	103	*93*
	60			91	*83*	101	*91*
	40			76	***68***	72	*66*
	20	124	*97*	41	***38***	52	***51***
	0	119	*88*	29	*20*	42	***36***
	-20	99	*78*	27	*11*	27	*15*
	-40	68	***57***				
	-60	48	***38***				
B	80			106	*93*	119	*98*
	60			113	*97*	111	*93*
	40			74	***63***	92	*75*
	20	135	*100*	45	***39***	69	***58***
	0	130	*100*	36	*30*	42	***34***
	-20	100	*77*	30	*12*	31	*20*
	-40	107	***83***				
	-60	53	***37***				

longitudinal direction	T	Surface KV	Surface *DF*	1/2 R KV	1/2 R *DF*	Axis KV	Axis *DF*
	°C	J	%	J	%	J	%
H	80			57	68	77	88
	60			50	**55**	66	74
	40	107	92	45	**48**	53	**60**
	20	103	93	33	29	44	**44**
	0	97	**85**	31	17	32	24
	-20	47	**43**				
	-40	75	70				
	-60	37	22	17	0	21	4
C	80			67	77	73	83
	60			50	**53**	54	66
	40	113	100	41	**43**	51	**54**
	20	100	90	32	26	35	**36**
	0	86	74	20	9	31	23
	-20	72	**69**				
	-40	50	**45**				
	-60	37	23	16	0	14	0
B	80			69	88	57	70
	60			53	**63**	78	72
	40	106	98	47	**48**	58	**52**
	20	91	90	37	34	36	**32**
	0	76	76	21	10	36	24
	-20	85	81				
	-40	54	52				
	-60	62	**53**	13	0	15	1

Table 7: Material hardness on the cross-section of the forgings – the average from the heats EU1, EU2 and EU3
Table 7: Trdota materiala na prečnem prerezu izkovkov – povprečje talin EU 1, EU 2 in EU 3

$HBW_{5/750}$	surface	◄direction surface		1/2 R	direction axis ►		axis
sample range distance from the surface of the forging (mm)	0 to 40	41 to 80	81 to 120	121 to 160	161 to 200	201 to 240	240 to 280
H	301	290	290	292	294	292	297
C	300	283	282	286	285	286	288
B	309	295	285	282	283	283	282

A second method for the evaluation of the mechanical properties of the rotor forgings was the determination of the FATT T_{50}, i.e., the Fracture Appearance Transition Temperature, defined by the ratio 50 % of brittle and 50 % of ductile fracture.

The results obtained for these tests in the longitudinal and transversal directions are given in **Table 6** with the transition from ductile fracture to brittle fracture being highlighted.

These results confirm that a satisfactory FATT T_{50} transition temperature at the surface part of the rotor forging was obtained.

The values of the transition temperature are lower for the interior parts of the forging, with a higher toughness in the axial part than in the zone 1/2*R*, at half the distance between the forging surface and the centre. The transition temperature of the FATT T_{50} can be obtained by an approximation in the diagram *KV* – *DF*.

4 HARDNESS

The hardness *HB* was determined on the cross-section of the forgings from the heats EU1, EU2 a EU3, and the results are given in **Table 7**.

Figure 2 shows graphically the average values of the hardness on the cross-section of the forgings. The highest hardness was achieved for all three forgings at the surface.

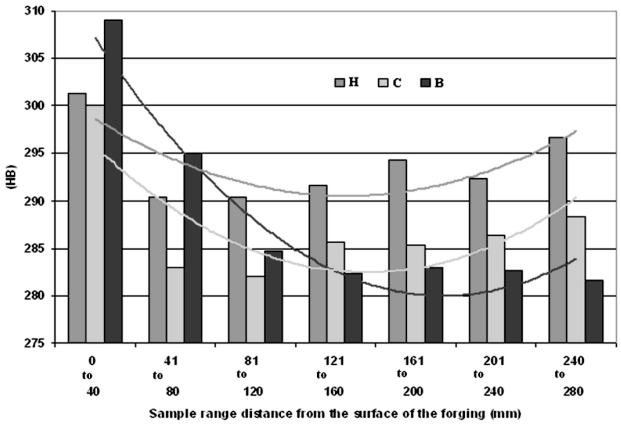

Figure 2: Average hardness on the cross-section of the forgings from the heats EU1, EU2 and EU3
Slika 2: Povprečna trdota na preseku izkovkov

5 CONCLUSIONS

The mechanical properties were determined on the cross-sections of the test forgings from the experimental heats. These properties show certain trends with respect to the position on the forging in the cross-section.

In longitudinally oriented samples, in comparison with transversally oriented samples, higher values of the mechanical properties were determined from a tensile test at room temperature; in the longitudinal direction from an average of three forgings the following satisfactory properties were achieved on the surface of the forgings: $R_{p0,2}$ = 827 MPa, R_m = 955 MPa, A_5 = 17.1 %, Z = 65.8 %. The other values in the direction towards the forging axis show, from the viewpoint of the yield point and the strength, a lower material strength and also lower plastic properties, defined by the ductility and the contraction.

The notch toughness of the steel, defined as the peak load during the impact test at room temperature, was in the range of *KV* = 80 J to 136 J in the longitudinal direction and of *KV* = 106 J to 151 J in the transversal direction. The share of ductile fracture *DF* = 83 % to 98 % in the longitudinal direction and *DF* = 90 % to 100 % in the transversal direction confirms that the notch toughness at the surface of the forging was better in the transversal direction. The values of the peak load decrease sharply from the surface towards the axis of the forging. At a distance of ½ the shaft radius the following values were obtained in the transversal direction: *KV* = 34 J to 55 J at *DF* = 28 % to 50 %, and in the forging axis: *KV* = 50 J to 91 J at *DF* = 48 % to 83 %. The steel has a better notch toughness in the axial part of the forging than in the middle radius.

The values of the yield point and the tensile strength of the experimental forgings document mutually comparable properties with a low dependence on the place from where the sample was taken. Greater differences in the longitudinal and transversal directions were found, particularly for the values of the transition temperature FATT T_{50}.

The obtained mechanical properties of the experimental rotor forgings made of the 26NiCrMoV115 steel indicate the necessity for a further improvement in the forming process and the heat treatment.

The transition temperatures of the FATT T_{50} determined by considering the peak load *KV* (J) and the share of ductile fracture on the fracture surface *DF* (%) show a change in the steel's plastic properties. The lowest transition temperature was always found for the surface of the forging. In all cases a lower transition temperature was achieved in the axial part in comparison with the part at the middle radius of the rotor forging. No important differences related to the position of the sample in the original ingot were found.

The hardness on the forging cross-section is in agreement with the changes of the mechanical properties. A significant drop of hardness was found at a distance of 40 mm below the forging surface, while the changes related to the axis direction are insignificant. The highest average hardness of *HB* 294 was achieved at the place corresponding to the part under the ingot end, a lower average hardness of *HB* 288 was found in the footing part, and a comparable average of *HB* 287 was achieved in the central part of the forging, i.e., of the original ingot.

The comparison of the scatter of the mechanical properties indicates an acceptable anisotropy of the mechanical properties.

6 LITERATURE

[1] Balcar, M., Sochor, L., Martínek, L., Turecký, V. a kol: Mechanical properties of forgings made of steel 26NiCrMoV115, heats EU1, EU2 and EU3. Progress report for solution of the project E!3192 ENSTEEL. Žďár nad Sázavou. 2006, 16 p

[2] Němeček, S.: Heat treatment of rotor steels. Report No. Z-2006/059. COMTES FHT, s.r.o. 2006, 15 p

[3] Kvačkaj, T.: Progress report of the project EUREKA E!3192 ENSTEEL. Technical University Košice. 2005, 14 p